Alexandria Engineering Journal 104 (2024) 246–260

Contents lists available at ScienceDirect

Alexandria Engineering Journal

journal homepage: www.elsevier.com/locate/aej

Comprehensive investigation of microwave sintered AlCoCrFeNi/Ti-6Al-4V composite: Microstructural insights, mechanical properties, and tribological performance

Mahesh Mandapalli [a], U.V. Akhil [a], N. Radhika [a,*], L. Rajeshkumar [b]

[a] Department of Mechanical Engineering, Amrita School of Engineering, Coimbatore, Amrita Vishwa Vidyapeetham, India
[b] Center for Research, Alliance University, Anekal - Chandapura Road, Bengaluru, Karnataka 562106, India

ARTICLE INFO

Keywords:
Ti-6Al-4V
High entropy alloys
AlCoCrFeNi
Microwave sintering
Tribology

ABSTRACT

Ti-6Al-4 V is an extensively used and highly versatile titanium alloy. It is renowned for its lightweight-to-strength ratio, excellent biocompatibility, and corrosion resistance. The pursuit of advanced materials with enhanced mechanical strength, and wear resistance has led to the exploration of high entropy alloys (HEA) as particle reinforcements. This study combines Ti-6Al-4 V with AlCoCrFeNi HEA at different weight compositions (0 %, 2 %, 4 %, 6 %, 8 %) to create novel composites with tailored properties. The composites were subjected to density, microhardness, tensile, and pin-on-disc tests to evaluate mechanical and tribological properties. Microstructural analysis revealed that microwave sintering has enhanced densification and resulted in uniform dispersion of HEA particles within the Ti-6Al-4 V matrix. The XRD and EBSD analysis revealed the presence of BCC structure in the composite. 8 wt%-AlCoCrFeNi/Ti-6Al-4 V sample exhibited an impressive 81.66 % increase in microhardness and 21.23 % in yield strength, compared to the base sample. Furthermore, noteworthy reductions of 45 % in wear rate and 40 % in coefficient of friction (COF) when subjected to tribological analysis. The worn surface revealed the presence of oxide layer formation at elevated sliding velocity and distance which resulted in reduced wear rate.

1. Introduction

Titanium and its alloys are recognized for their lightweight nature, exceptional strength, ability to resist corrosion and outstanding compatibility with biological systems. The most used titanium alloy is Ti-6Al-4 V due to its outstanding mechanical properties and feasible machinability [1,2]. They exhibit excellent creep resistance and fatigue resistance due to their ability to form complicated multiscale hierarchical structures [3]. Despite the variations in structures and strength, along with the presence of a protective oxidation layer, in applications involving their tribological properties, these alloys are not preferable. Their lack of efficiency is contributing to a decrease in the usage of alloys in the current industry for prolonged tribological applications [4,5]. A comparative study of untreated β-annealed alloys showed that their wear resistance was higher when the applied loads were less than 2 N because of their super elasticity effect, and at loads > 2 N the wear rate exhibited a significant increment compared to the as-received alloy [6]. Therefore, most industries are using composites as an alternative.

Metal matrix composites (MMC) are the materials that are most suitable to withstand high temperature environments and different structural loading conditions. The traditional materials are replaced by Titanium Matrix Composite (TMCs) due to their superlative features like weight reduction while still maintaining the same high strength [7,8], corrosion, and wear resistance [9,10]. When Ti-6Al-4 V was reinforced with 0.5 wt% of nickel-phosphorus decorated graphene nanoflakes, the yield stress of the material increased by 1.3 folds while still maintaining 34.2 % ductility [11]. Ti/Zr-based bulk glass metallic composite reinforced with 15 at% of Cu exhibited an increased hardness of 437HV with a significant reduction in plasticity [12]. Using ceramics as reinforcement an MMC exhibits both ductile and brittle characteristics making it an excellent material [13]. TiC, TiB, and TiN are typically employed as reinforcing agents in TMC. The addition of TiC particles and TiB whiskers as reinforcements in the Ti matrix, produced through powder metallurgy (PM), resulted in a remarkable enhancement in tensile strength, increasing from 654 MPa to 1130 MPa [14]. However, using ceramics as reinforcements has led to a decrease in their toughness, and

* Corresponding author.
E-mail address: n_radhika1@cb.amrita.edu (N. Radhika).

https://doi.org/10.1016/j.aej.2024.06.067
Received 10 March 2024; Received in revised form 19 June 2024; Accepted 23 June 2024
Available online 26 June 2024

tensile ductility [15–17]. Ceramic particle fraction was increased to increase wear resistance, but this led to the formation of a weak interface with low strength which resulted in poor bonding and the spalling of the reinforcement [18] and further using TiN resulted in low wear rates and lower coefficient of friction [19]. Therefore, HEAs are used as reinforcement to improve the tribological properties and strength without decreasing other mechanical properties.

HEAs are alloys having 4 or 5 elements as the principal elements with almost equal composition (generally 5–35 %) [20,21]. Their ability to influence solid phase solution stability through configurational entropy control has earned the name HEA and they also exhibit extraordinary strength at high temperatures, structural stability, and high strength due to the four core effects that happen in them including high entropy effect, lattice distortion effect, sluggish diffusion effect, and cocktail effect [22–24]. They are generally synthesized using the gas atomization (GA) process to obtain a homogenous structure and an even spread of elements for surface modifications [25,26] or by mechanical alloying (MA) to extend the solid solubility of the simple solid structures of HEA for immiscible systems and to produce Light weight HEA's [27,28]. Therefore, MMCs with HEA as reinforcement are expected to overcome the limitations of traditional reinforcements. When the Al matrix was reinforced with $CoNiFeCrAl_{0.6}Ti_{0.4}$ prepared by combined ball milling, hot pressing, and hot extrusion, the HEA particles were observed to have uniformly distributed contributing to the grain refinement resulting in excellent thermal stability and high hardness when compared to the ceramic reinforced matrices [29].

The powder mixture is compacted and sintered in PM to transform it into a solid form. Ti alloys are generally sintered via conventional sintering and hot isostatic pressing (HIP). Conventionally sintered Ti alloys cannot match the mechanical and microstructural properties of the wrought Ti [30]. HIP is mainly used to minimize the defects but not to remove them. Also, using this method leads to an increase in ductility but not in strength [31]. Hence microwave sintering can be used as an alternative for enhanced properties. Microwave sintering reduces sintering time due to higher heating rates. Direct absorption of microwaves causes uniform volumetric heating and higher diffusion rates, resulting in a uniform microstructure and higher density [32]. Ti6Al6V2Sn reinforced with 0.5 wt% Gn and fabricated by microwave sintering has shown the relative density to be 94 % with refined grains resulting in enhanced mechanical properties [33]. Microwave sintering at 1200°C yielded the Ti-3Al-2.5 V-2WC composite with 98 % relative density in comparison to conventional sintering. The COF was observed to be 0.42, showcasing enhanced wear resistance attributed to the WC reinforcement [34]. Microwave sintered materials when compared with conventional sintered ones, exhibited uniform shrinkage in all 3dimensions [35], higher hardness [35,36], enhanced toughness [36,37] and in addition better corrosion and erosion resistance [35] than the latter ones. Therefore, the method used to fabricate the reinforced material affects the particle distribution of the HEA, which, in turn, affects the mechanical and tribological properties.

The ongoing focus of our research involves developing a material that incorporates Ti-6Al-4 V and AlCoCrFeNi HEA, utilizing PM in conjunction with microwave-assisted sintering. Following the successful synthesis of the material, its microstructure was analyzed using Scanning Electron Microscopy (SEM). Additionally, Energy Dispersive X-ray spectroscopy (EDS) was employed to determine its elemental composition, X-ray diffraction Analysis (XRD) was performed to investigate its phases, and to further analyze the crystal structure, Electron Backscattering Diffraction (EBSD) was conducted. The material's mechanical and tribological properties were evaluated by examining its microhardness via Vickers hardness tester and wear rate utilizing pin-on-disc apparatus. In the end, an assessment of the worn surface morphology was performed to deduce the wear mechanism.

2. Materials and methods

2.1. Sample preparation

A commercial Ti-6Al-4 V powder was taken as the base matrix and equiatomic AlCoCrFeNi HEA synthesized using GA process was used as the reinforcement. In addition, using GA process involves usage of lot of variable parameters [38] which in turn produces more control on the particle size and the regular sphere shape particles are produced instead of irregular ones. High energy ball milling on the other hand can cause agglomeration of powder particles and is more prone to contamination which can directly affect the final properties of HEA [38]. In the AlCoCrFeNi HEA, Al acts as the BCC/B2 stabilizer, enhancing the mechanical properties. Co introduces disorder by promoting the BCC phase, while Cr and Fe work to minimize the mismatch of crystallographic structures between the BCC and B2 phases. Ni plays a role in providing solid solution strengthening, effectively reducing the brittleness of the alloy [39]. Therefore, providing AlCoCrCrFeNi as reinforcement for a titanium matrix is expected to have better results regarding mechanical and tribological properties. Therefore, both the powders were mixed in a low-energy ball milling for 1 h to obtain a homogenous composition. Various composite samples were created by incorporating different weight percentages (2 %, 4 %, 6 %, and 8 %) of HEA, in addition to the base sample (Ti-6Al-4 V), serving as the reference material. The resulting samples are compacted to produce a solid mass by applying a pressure of 950 MPa with the help of a hydraulic press. The resulting mass was sintered by microwave sintering for 1 h at 850°C, with the help of 2.45 GHz 5 kW microwave equipment.

2.2. Composite evaluation

The properties of the HEA powder and sintered samples were thoroughly analyzed utilizing advanced equipment. A Carl Zeiss Inverted Metallurgical Microscope, equipped with a 12 V/100 W Halogen lamp for illumination, was used to analyze the optical microstructure. Simultaneously, SEM analysis and constituent elements study were performed using a Carl Zeiss Electron Microscope with EDS, while the structural phases were analyzed through XRD in a scan range of 0°-90°. For an even more precise analysis of grain boundaries and crystallographic orientation, EBSD was utilized. The density of the samples was determined both theoretically and experimentally along with porosity by the principle of Archimedes (ASTM D792 standard). The microhardness was evaluated with the help of a diamond intender by applying a 100 g load for 15 sec using a Vickers hardness tester (ASTM E92 standard). The test was conducted on each sample five times, and the average value was used for analysis. The tensile test was conducted at room temperature at a crosshead speed of 0.5 mm/min and the fracture surfaces were analyzed using SEM. To analyze COF and wear rate, a pin-on-disc test was performed with a load of 10–40 N, a disc velocity of 0.5 m/s - 3.5 m/s, and a sliding distance of 500–2000 m (ASTM G99–05 standard). The worn surface morphology was evaluated by analyzing worn surfaces with the help of SEM. Fig. 1 provides a pictorial representation of the methodology.

3. Results and discussion

3.1. Microstructural characterization

The morphological evaluation of AlCoCrFeNi HEA has been illustrated in Fig. 2. The HEA particles were observed to be spherical, exhibiting a consistent and homogenous morphology with a mean particle size of 20μm Fig. 2(a). The EDS analysis of the HEA validated the existence of the relevant elements which are illustrated in Fig. 2(b). All the 5-elemental compositions (Al, Co, Cr, Fe, Ni) in the HEA turned out to be almost 20 at% proving the uniform distribution of HEA elements. The results also confirm that no foreign substance was present,

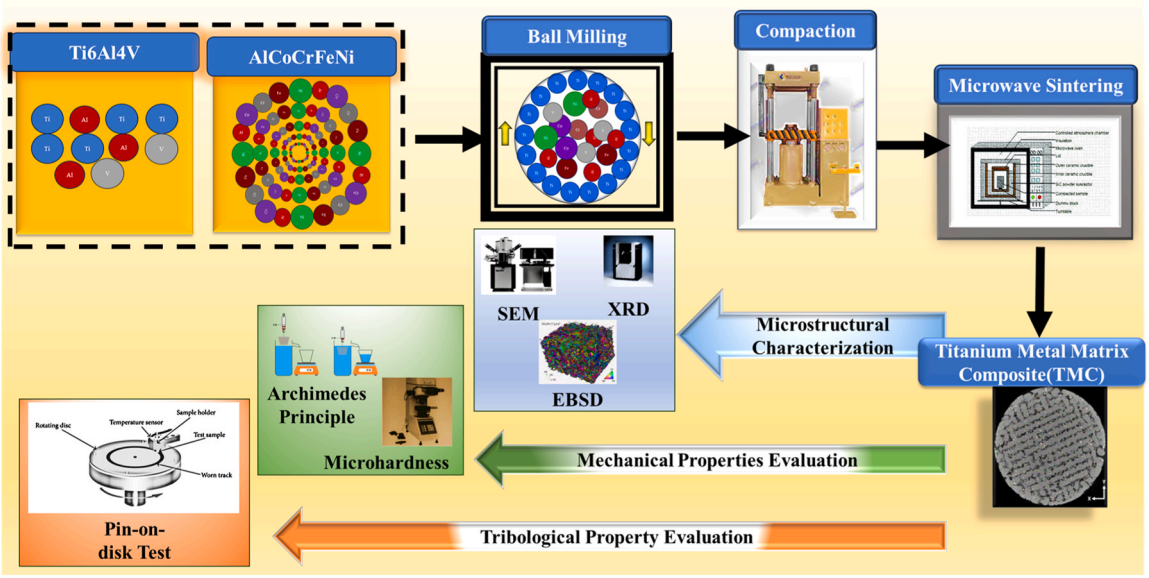

Fig. 1. Visual schematic detailing the methodology.

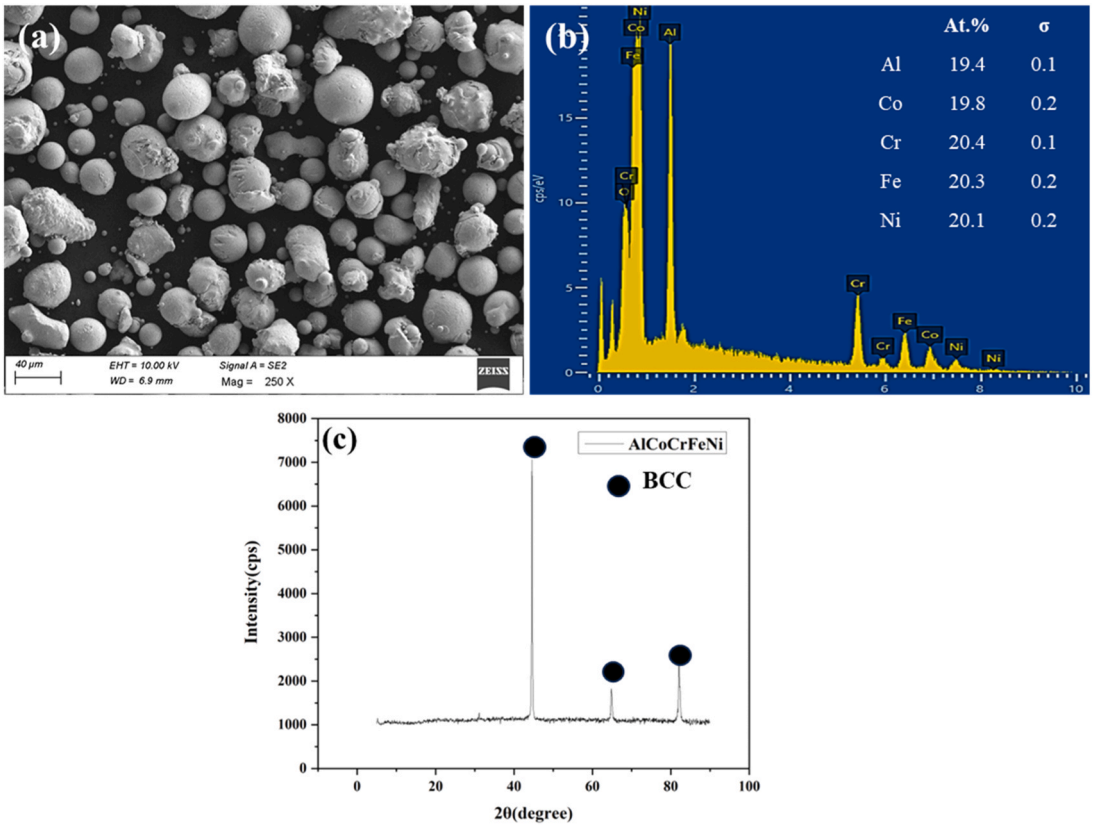

Fig. 2. (a) SEM image (b) EDS (c) XRD diffractogram of AlCoCrFeNi powder.

confirming the purity of the powder. The XRD patterns of AlCoCrFeNi in Fig. 2(c) showed 3 peaks, representing BCC structures that are in the (110), (200), and (211) planes of orientation respectively. This points towards the establishment of a solid solution that is stable and uni -phasic.

Fig. 3(a–e) depicts the metallographic images of Ti-6Al-4 V and AlCoCrFeNi reinforced Ti-6Al-4 V samples of different wt% composition. It was observed from these images that AlCoCrFeNi particles were dispersed into the Ti-6Al-4 V matrix in an almost uniform manner, and they bonded well at the interface. HEA particles are visible in almost circular shapes scattered across the interface layer. The surface of the sintered samples was devoid of any cracks or pores. The SEM images of Ti-6Al-4 V along with the AlCoCrFeNi/Ti-6Al-4 V samples are shown in Fig. 4(a-e). In Fig. 4(b-e), the reinforcement particles were strongly bonded with the matrix alloy. Structural variations in shape amid the matrix and HEA particles, along with a significant proportion of HEA particles, contributed to the minimized occurrence of voids.

Fig. 5(a,b) depicts the observations from EDS study, illustrating the

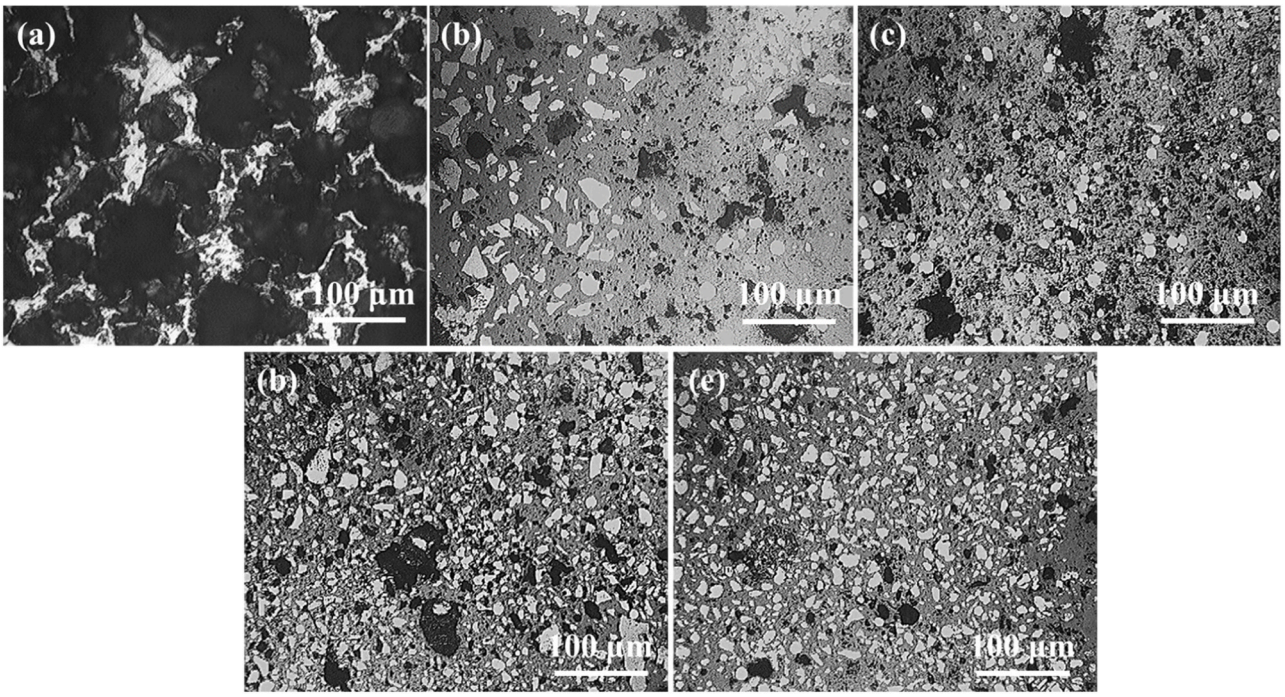

Fig. 3. Optical microstructures of TMC's (a) Ti-6Al-4 V (b) 2 wt%-AlCoCrFeNi/Ti-6Al-4 V (c) 4 wt%-AlCoCrFeNi/Ti-6Al-4 V (d) 6 wt%-AlCoCrFeNi/Ti-6Al-4 V (e) 8 wt%-AlCoCrFeNi/Ti-6Al-4 V.

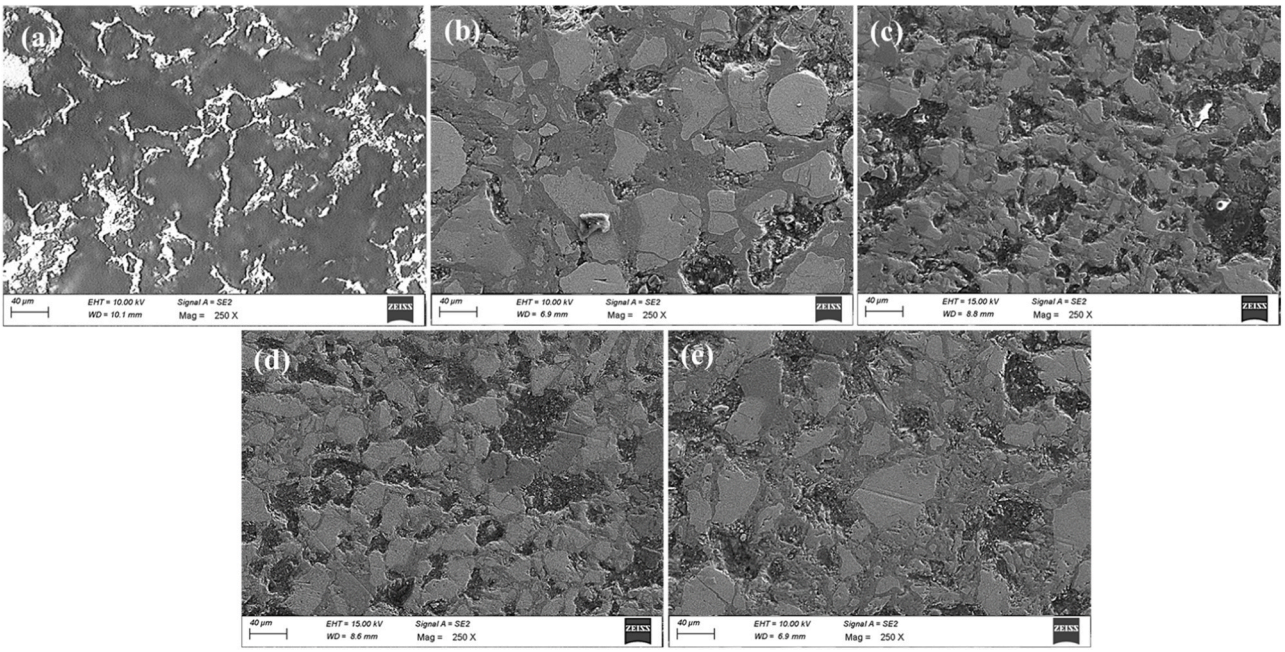

Fig. 4. SEM Images of TMC's (a) Ti-6Al-4 V (b) 2 wt%-AlCoCrFeNi/Ti-6Al-4 V (c) 4 wt%-AlCoCrFeNi/Ti-6Al-4 V (d) 6 wt%-AlCoCrFeNi/Ti-6Al-4 V (e) 8 wt %-AlCoCrFeNi/Ti-6Al-4 V.

elemental composition of both Ti-6Al-4 V and 8 wt%-AlCoCrFeNi/ Ti-6Al-4 V. The findings from the base sample closely correspond to the nominal composition of Ti-6Al-4 V [40]. Fig. 5(c,d) depicts the elemental mapping of the base sample and 8 wt %-AlCoCrFeNi/Ti-6Al-4 V sample. The 8 wt%-AlCoCrFeNi/ Ti-6Al-4 V, revealed the presence of elements such as Al, Co, Cr, Fe, Ni, V and Ti, it was also observed that the HEA was homogenously distributed within the matrix (Fig. 5(d)).

The XRD analysis of the sintered samples is illustrated in Fig. 6. The base sample's diffractogram confirmed the presence of αTi (ICDD: 00–001–1198) which is stabilized by the presence of the aluminum and βTi (ICDD: 01–089–4913) which is stabilized by the presence of vanadium. The reinforced samples were observed to have BCC (ICDD:006–696) peak due to the presence of AlCoCrFeNi, which increased with the increment in wt% of HEA reinforcement, beside αTi in the diffractogram. A slight augmentation in the βTi peak was also observed due to the presence of Fe, Ni and Cr in HEA, stabilizing β-phase. The αTi peak did not vary since the only element present in the

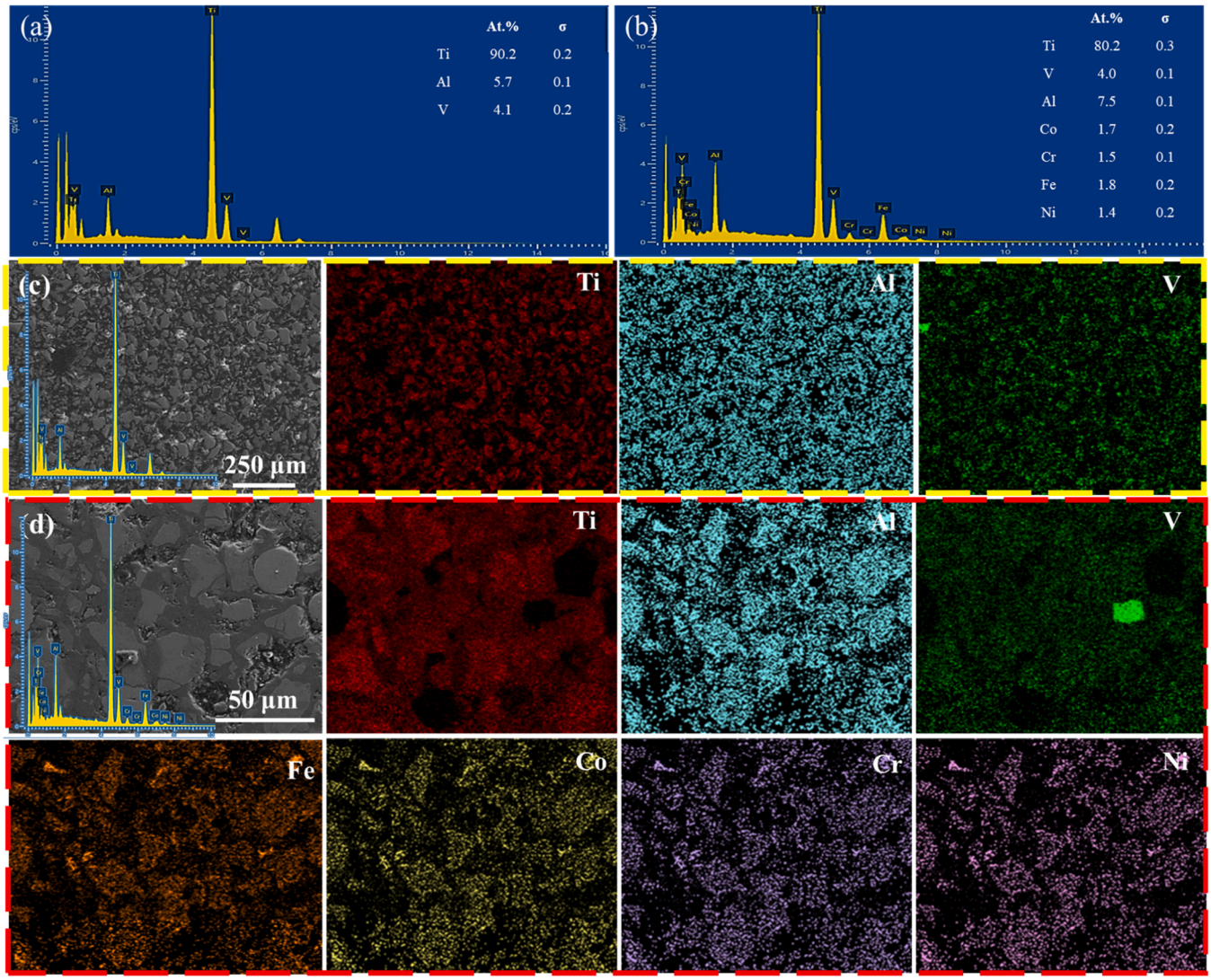

Fig. 5. EDS image of (a) Ti-6Al-4 V (b)8 wt%-AlCoCrFeNi/Ti-6Al-4 V and elemental mapping of (c) Ti-6Al-4 V (d) 8 wt%-AlCoCrFeNi/Ti-6Al-4 V.

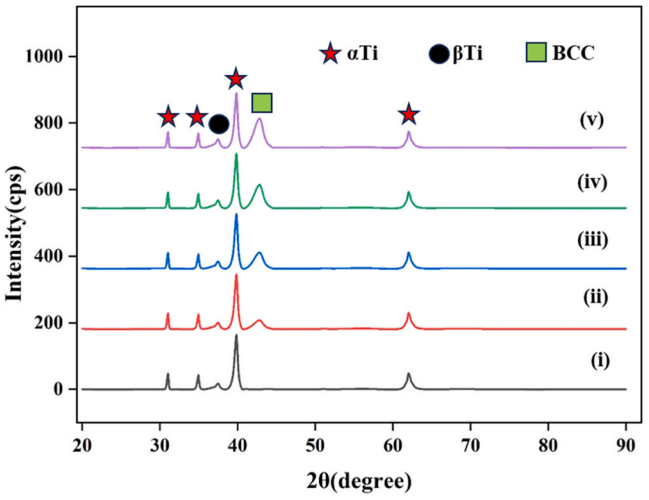

Fig. 6. XRD patterns of (i) Ti-6Al-4 V (ii) 2 wt%-AlCoCrFeNi/Ti-6Al-4 V (iii) 4 wt%-AlCoCrFeNi/Ti-6Al-4 V (iv) 6 wt%-AlCoCrFeNi/Ti-6Al-4 V (v) 8 wt %-AlCoCrFeNi/Ti-6Al-4 V.

HEA that stabilizes the α-phase is Al.

The results of EBSD analysis of the 8 wt%AlCoCrFeNi/Ti-6Al-4 V are illustrated in Fig. 7. The crystallographic orientation mapping of the AlCoCrFeNi/Ti-6Al-4 V sample with different colors has been provided in Fig. 7(a). The image indicating the phases of Ti and HEA reinforcements has been depicted Fig. 7(b). Red colors represent the BCC structure (β-Ti and HEA) and green color represents the α-Ti phase (HCP). Titanium(α-Ti) is about 76.5 % and the BCC structure is about 23.5 %. The α-Ti phase was observed to be dominating as Al present in the base and the HEA acts as an α-stabilizer promoting the alpha phase growth in the sample [41]. Fig. 7(c) represents the Kernel Average Misorientation (KAM) of the reinforced sample, 0^0 being the lowest angle is represented in blue whereas the maximum angle of 4.99° is represented in red. From the image, it is concluded that the majority of grain boundaries are aligned as they are of the same crystallographic orientation α-Ti, and only very few are aligned in the crystallographic orientation of BCC. The alignment between these two structures is minimal. The interaction between the microwaves and the electrically conductive particles in the powder resulted in volumetric heating which in turn resulted in more uniform and rapid temperature distribution throughout the material, minimizing temperature gradients and reducing the opportunity for grain growth. Thus, following the well-established Hall-Patch effect, there is an expectation for the material to possess improved hardness and resistance to wear. Fig. 7(d)

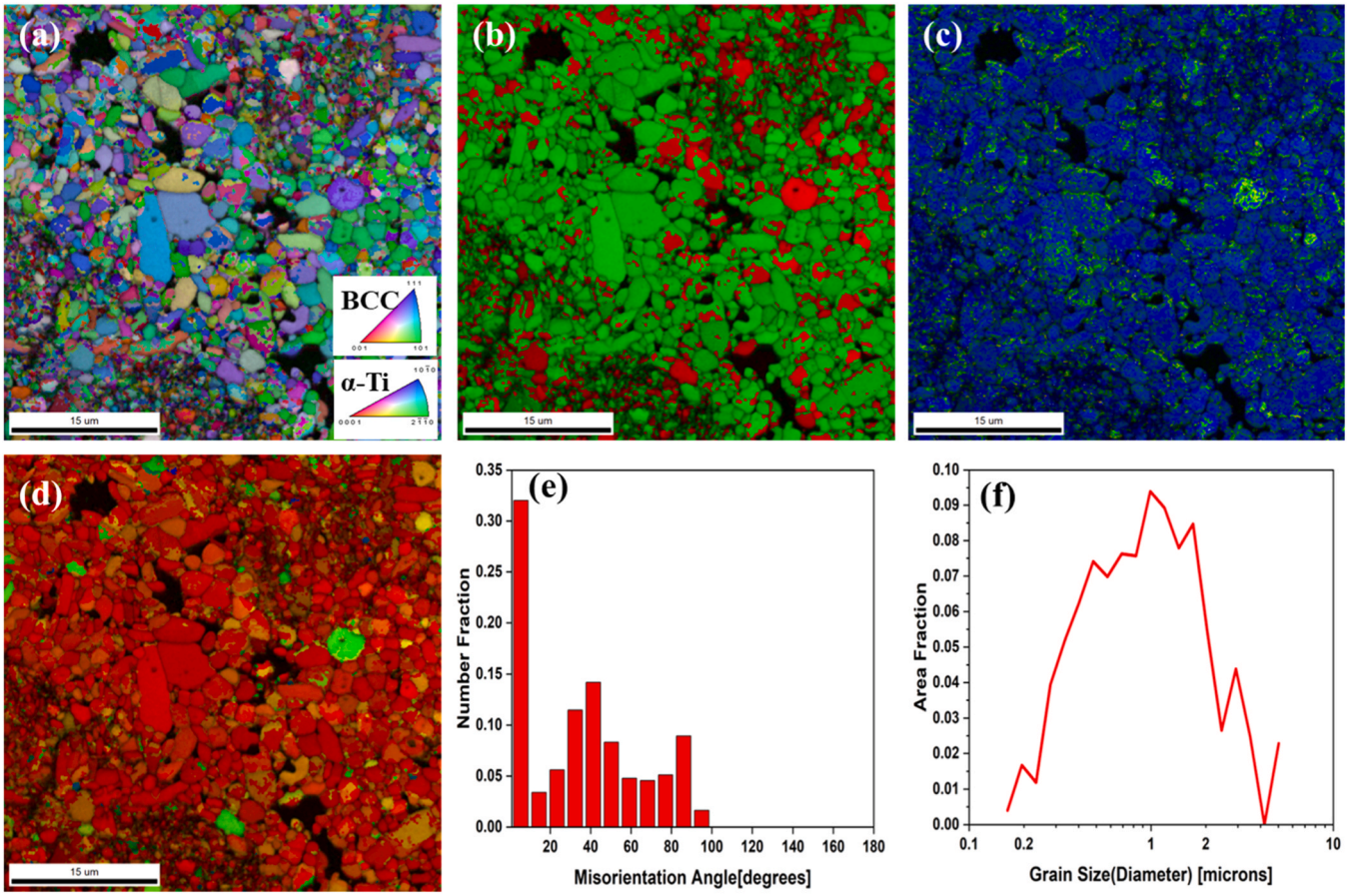

Fig. 7. EBSD results of 8 wt%AlCoCrFeNi/Ti-6Al-4 V (a) Grain distribution mapping (b) phase mapping (c) KAM mapping (d) Schmid Factor mapping (e) Area fraction vs Misorientation angle (f) Distribution of Grain Size(μm).

represents the Schmid Factor (SF). The minimum value of SF in the reinforced sample was observed to be 0.315 which is represented in blue, and the maximum value of SF was 0.5 which is represented in red. From the figure, it indicates that a major portion of the sample is more prone to dislocation movement. The existence of strain fields containing higher quantities of dislocations is a key factor in improving mechanical properties [42]. Fig. 7(e) represents the graphical distribution of the number of grains having the same misorientation angle. 35.4 % grain distribution has a lower angle grain boundary (LAGB) and 63.2 % grain distribution has a higher angle grain boundary (HAGB). Fine grain structure and HAGB can impede the dislocation movement which can result in a continuous increase in the mechanical properties and the tribological properties [43]. In 8 wt%- AlCoCrFeNi/Ti-6Al-4 V, the mean grain size was found to be 1.2μm (Fig. 7(f)). HEA particles can impede dislocation slip and induce grain rotation towards a more stable orientation, since the reinforced sample is a polycrystalline material, each of the phases has been analyzed individually.

Fig. 8 represents the EBSD results of the BCC structure phase. The rotation angle distribution of crystal lattices concerning the standard BCC orientation angle is illustrated in Fig. 8(a). The red points and the red line represent the crystal lattice which has a minimum rotation angle of 1°. By this statistical condition, there are a total number of 24,486-grain boundaries having BCC as the crystal lattice. Fig. 8(b) represents the SF distribution. The BCC crystal lattices show a minimum of 0.317 and a maximum of 0.5 SF. The variation is because the BCC structure allows for a greater degree of freedom in grain growth, resulting in different grain sizes (larger, elongated) which in turn causes variations of dislocation movements compared to α-Ti resulting in different SFs. The orientation of the BCC structures is described in Fig. 8(c-e) with the help of pole figure (PF) and orientation distribution function (ODF). From Fig. 8(c), it is observed that most BCC structures are oriented in the directions of [0 0 1] and [1 1 1] which is found in compressed BCC alloys [44]. Fig. 8(d) and (e) represent PF and ODF figures which took the sample symmetry as Triclinic and calculations by Harmonic Series expansion exhibiting a maximum Harmonic texture of 3.96 in PF and 2.75 in ODF.

Fig. 9 depicts the EBSD outcomes related to the α-Ti (HCP) structure. The distribution of rotation angles of crystal lattices concerning the standard orientation angle is portrayed in Fig. 9(a). Employing analogous statistical criteria as applied in the BCC structural analysis, a total of 123,450 grains containing the α-Ti phase have been identified, confirming the predominant presence of the α-Ti phase in the reinforced sample. Fig. 9(b) illustrates the SF distribution, where the α-Ti crystal lattices exhibit a minimum of 0.422 and a maximum of 0.5 SF. The slight variation is attributed to the tendency of the HCP structure to form finer and more elongated grains, with grain formation in α-Ti alloys favoring a more equiaxed configuration, resulting in minimal differences in dislocations. Fig. 9(c) represents ODF mapping from which it is observed that the majority of α-Ti structures are oriented in direction $[2\ \bar{1}\ \bar{1}\ 0]$ due to the dislocation movements which is in agreement with previous work of near α-Ti alloy texture [45]. Fig. 9(d) and (e) represent PF and ODF figures which took the sample symmetry as Triclinic and calculations done by Harmonic Series expansion exhibited a maximum Harmonic Texture of 4.32 in PF and 4.26 in ODF.

3.2. Mechanical properties

Theoretical density determination for the samples was accomplished using the rule of mixtures, Fig. 10 depicts the graphical representation of the evaluated mechanical properties. When compared to the base

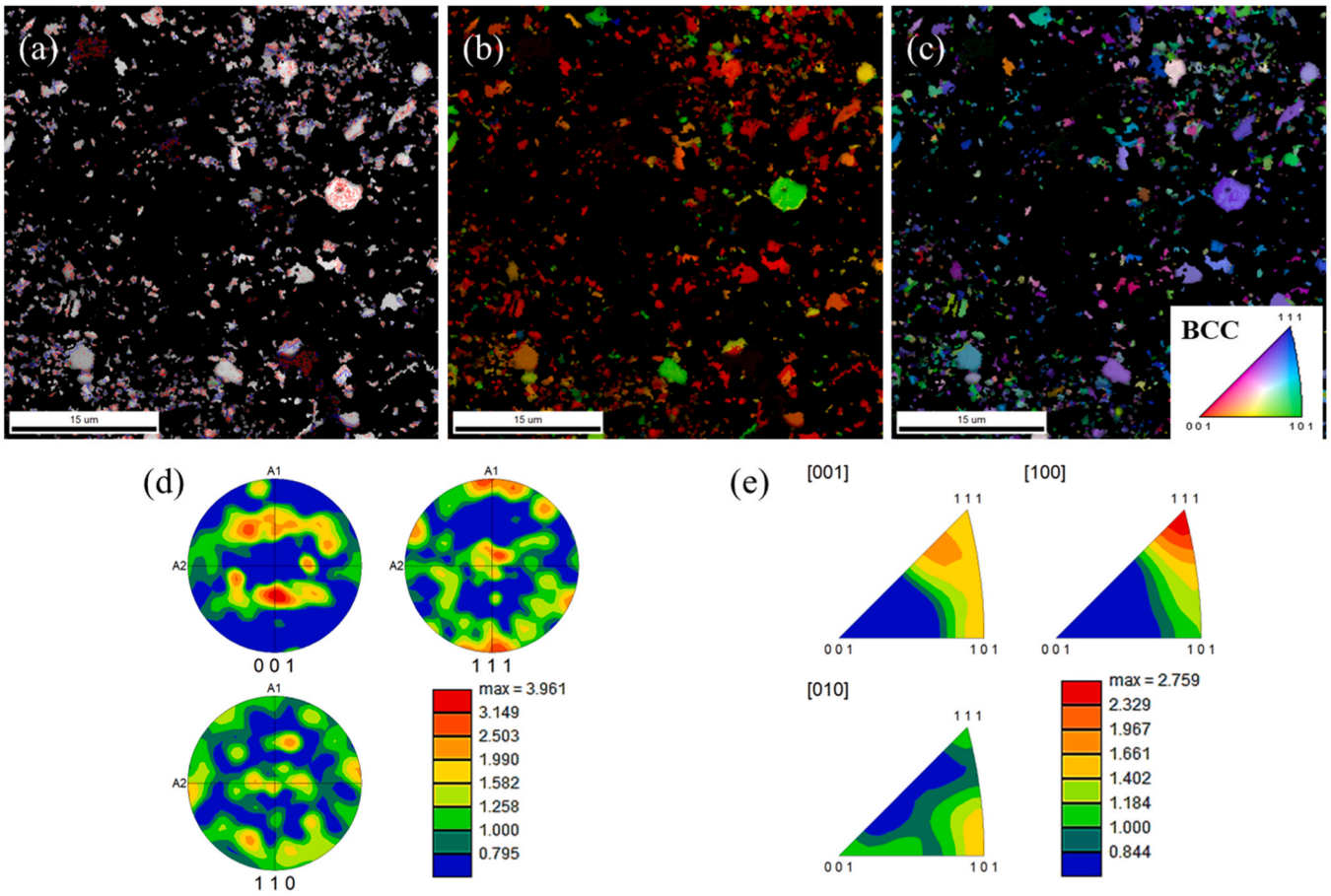

Fig. 8. Analysis of BCC structural phase (a) Grain distribution mapping of BCC structure (b) Schmid Factor mapping (c) Grain distribution of BCC based on orientational texture (d) Pole Figure of the BCC (e) Orientation distribution function figures of BCC.

sample, the reinforced sample values of density do not vary much implying that the Ti-6Al-4 V does not lose its lightweight property despite using HEA as a reinforcement. Most of the samples' relative density was around 94 % (Fig. 10 a,b), which concludes that microwave sintering leads to the development of material that has better density due to the instantaneous application of pressure and temperature that does not allow much room for the materials to outflow. Fig. 10(c) demonstrates the average hardness values of the samples along with the comparison. Comparative analysis with the base sample revealed a significant increase in hardness in the HEA-reinforced samples, facilitated by the even distribution of HEA particles and their strong bonding with the matrix. With the distribution of an increasing amount of HEA particles, there is a parallel escalation in the hardness levels of the composite. Therefore, the 8 wt% reinforced sample showed the highest increase in hardness among all other samples by 81.66 % when compared to the base samples. Also, at high temperatures, the bond formed between the Ti matrix and HEA is a strong diffusion bond due to the formation of the diffusion layer [46]. Increased hardness can also be accounted to the load transfer effect of AlCoCrFeNi, giving the composite a strong interface which in turn makes the composite exhibit excellent resistance during deformation to avoid failure and damage. An increase in the lattice distortion due to the presence of HEA particles and the grain refinement due to the reinforcement along with the increase in the number of grain boundaries, impedes the dislocation movement and also contributes to the increase in the hardness of the composite [33]. Microwave sintered 8 wt%.-AlCoCrFeNi/Ti-6Al-4 V exhibited improved hardness, compared to CoCrFeNiMo/Ti-6Al-4 V and $CoCrFeNiMo_{0.2}$/Ti composites by 53.1 % and 57.74 % respectively [46,47].

The engineering stress-strain values of the base sample and the reinforced samples derived at a typical room temperature are illustrated in Fig. 11. Similar to the case of hardness, the yield strength of reinforced samples significantly increases with reinforcement amount, exhibiting a parallel escalation in the values. The 8 %wt-AlCoCrFeNi/Ti-6Al-4 V reinforced sample showed the highest increase in yield strength by 21.23 % when compared to the base sample. Yield strength is a crucial fundamental performance characteristic among the particle-reinforced MMCs' mechanical and physical attributes. The yield strength of particle-reinforced metal matrix is regulated by various factors including the Orowan strengthening, load transfer effect, lattice friction stress, grain refinement strengthening (also known as Hall-Patch strengthening), solid solution strengthening and geometrically necessary dislocations strengthening [48–50] The Hall-Patch strengthening significantly enhances composite yield strength, followed by load transfer and geometrically necessary dislocation strengthening [47]. From the EBSD results, we observed a fine grain structure with a minimal KAM in the 8 wt% reinforced sample which can contribute to the display of its high strength along with relative proportions of α and β phases and the development in interface bonding. Fig. 6 demonstrates the XRD results, which revealed a slight increase in β peak with an increase in reinforcement of the HEA and from the EBSD results, the presence of the minimal amount of BCC (β phase) can be implied that the addition of the HEA reinforcement will not greatly diminish the base sample's shaping abilities.

The tensile fracture of the base sample and the reinforced samples are depicted in Fig. 12. Ductile fracture occurred in the samples under tensile deformation indicated by the appearance of tear ridges and pits. The base sample showed clear macroscopic plastic deformation before to fracture and there were different sized tear dimples near the fracture.

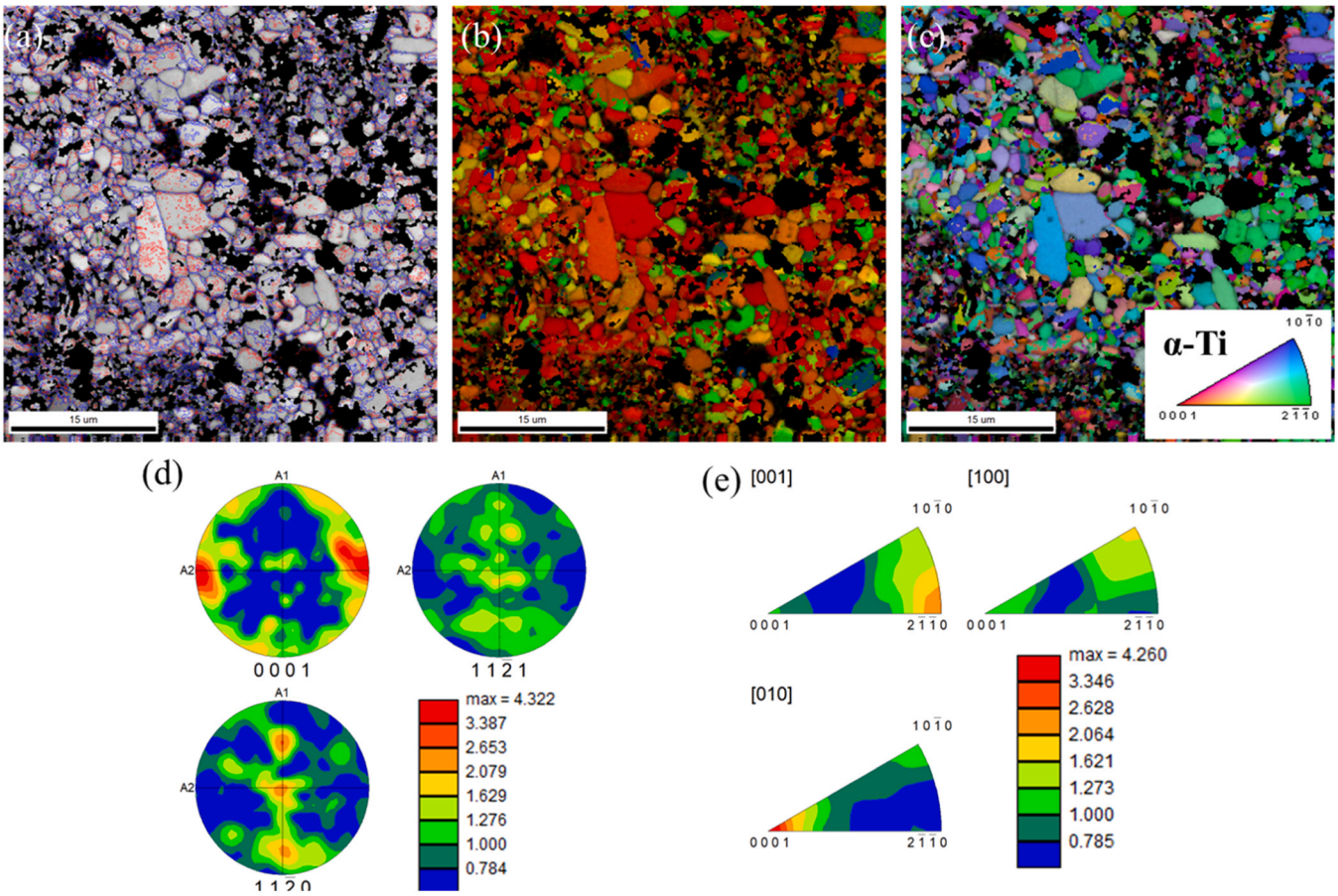

Fig. 9. Analysis of α-Ti (HCP) structural phase (a) Grain distribution mapping of α-Ti structure (b) Schmid Factor mapping (c) Grain distribution of α-Ti based on orientational texture (d) Pole Figure of the α-Ti (e) Orientation distribution function figures of α-Ti.

The increase in wt% of AlCoCrFeNi reinforcement resulted in a significant finer dimple, decreased area, and dulled tear ridge. This occurrence is attributed to the fact that ductility substantially reduces when wt% reinforcement increases. In the cracked surface of composites, both interfacial detachment and particle fractures were noted in this test. Ductile fracture of the base sample matrix, debonding of reinforcement matrix in the interface and fracture of reinforcement particles are the reasons for the deformation and fracture failure in the reinforced samples. A significant number of dimples surrounding the interdiffusion layer attested to good interface bonding, which is advantageous for preserving the reinforced samples' ductility (Fig. 12a-e). The matrix brittleness and the close hardness of the interdiffusion layer, facilitate better deformation coordination, resulting in HEA particles becoming stress concentration zones. The nanocrystalline region/interdiffusion layer evolved owing to the diffusion of solid solution and the diffused layer's intrinsic brittleness led to the creation of a mirror area. Dome-shaped region I is formed as a consequence of the interdiffusion layer and the reinforcement particles breaking apart (Fig. 12e').

3.3. Tribological properties

Figs. 11–13 illustrate how operational factors like sliding velocity, applied load, and sliding distance influence the wear rate and COF for the samples. The succeeding sections provide an analysis of the effects of operational factors on worn surfaces, with a focus on the impact of reinforced HEA particles.

3.3.1. Influence of applied load

Fig. 13 demonstrates the wear rate and COF of the base sample and the reinforced samples increased with an increment in the load which are applied at a constant velocity of 0.5 m/s and sliding distance of 500 m. 8 wt%.-AlCoCrFeNi/Ti-6Al-4 V exhibited the minimum wear rate of 2.1×10^{-4} mm^3/m with a COF of 0.2 at a load of 10 N which is increased linearly up to 5.9×10^{-4} mm^3/m with a COF of 0.36 at the load of 40 N whereas the base sample exhibited a wear rate of 8×10^{-4} mm^3/m with a COF of 0.34 at the load of 10 N which is increased linearly up to 1.1×10^{-3} mm^3/m with a COF of 0.58 at the maximum load of 40 N. The increment in the wear rate and COF at elevated loads can be credited to the increase in the contact pressure at higher loads. Table 1 presents the decrease in wear rate and COF for the reinforced samples at a maximum load of 40 N compared to the base sample under the same load. The increase in hardness is responsible for improving the wear resistance. The microwave energies lead to the formation of a strong interface between the matrix and reinforcement which contributed to the reduction in wear rate and the COF [34] With the increase in the wt% of the HEA reinforcements, more particles are evenly distributed which in turn strengthened the interface hence the wear rate was decreased significantly.

Fig. 14 depicts the morphological analysis of the worn surface of the 8 wt% AlCoCrFeNi reinforced Ti-6Al-4 V under applied load. Fig. 14(a) illustrates the worn surface of the samples exhibiting shallow groves and instances of particle pull-off which shows the manifestation of both adhesive and abrasive wear. This is attributed to the lower condition of 10 N. Minimal dislocation density leads to mild plastic deformation. The application of increased load causes a rise in dislocation density, leading to the detachment of small metal particles from the worn surface. This phenomenon contributes to a heightened wear rate, particularly evident when subjected to the maximum load of 40 N, as depicted in Fig. 14(b). The ongoing sliding motion of the removed materials along the rotating disc led to the continuous formation of deep grooves on the worn surface

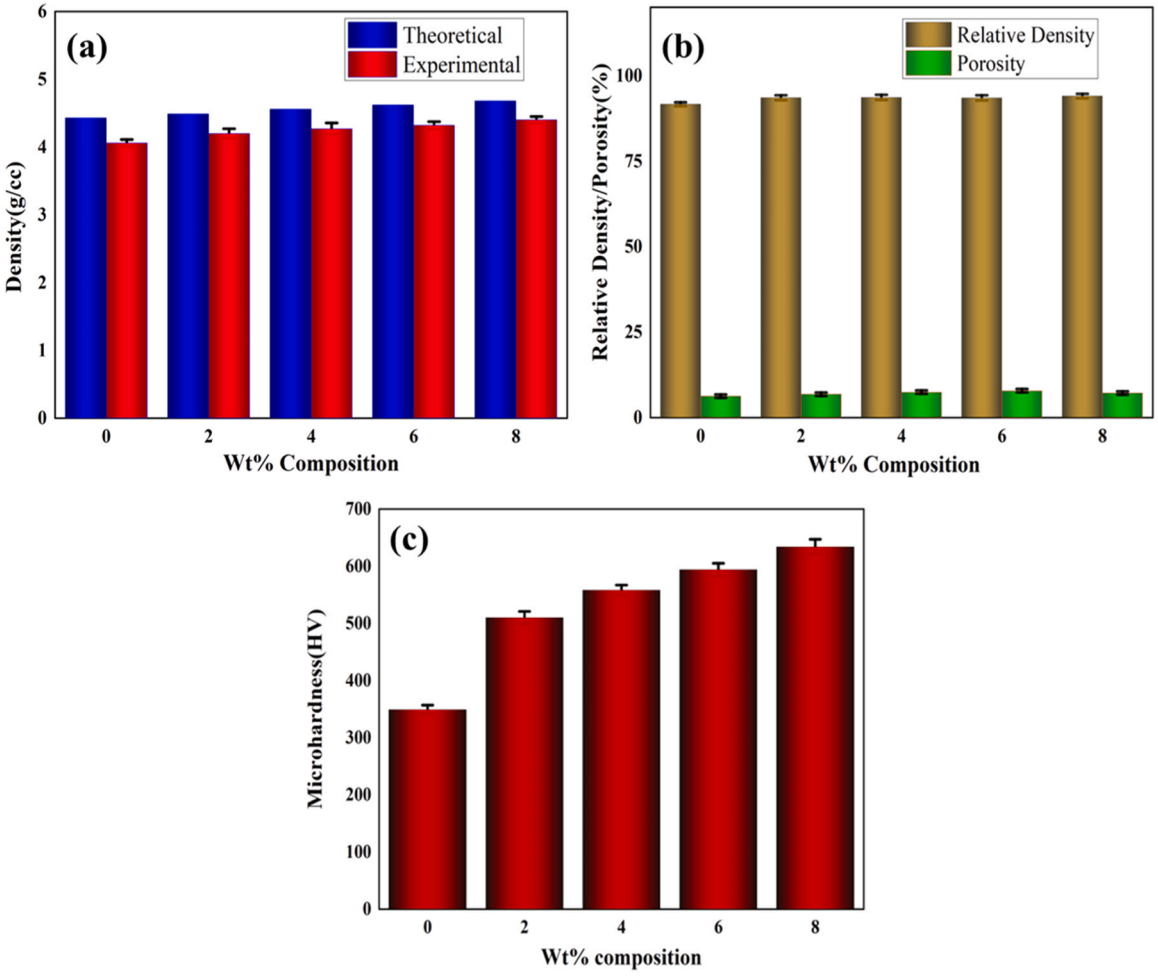

Fig. 10. Graphical Representation of the Mechanical Properties (a) Comparison of theoretical and experimental density (b) Comparison of relative density and porosity (c) Microhardness values.

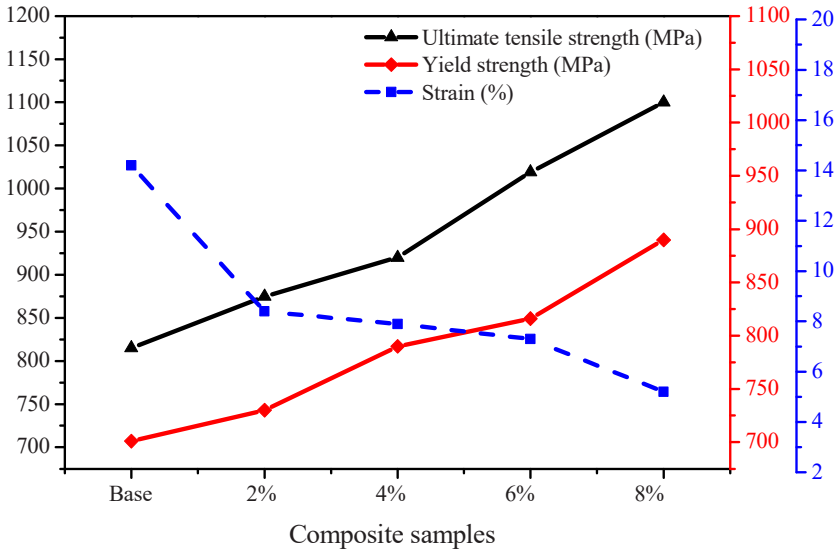

Fig. 11. Stress-strain data of composite samples.

of the reinforced sample. The pin surface adheres to the rotating disc as a consequence of severe plastic deformation caused by elevated frictional temperatures [51]. As a result, the softening process leads to the separation of metal particles from the reinforced sample. The induced plastic deformation increased with the augmentation of the applied load, resulting in the formation of deep and continuous grooves. The

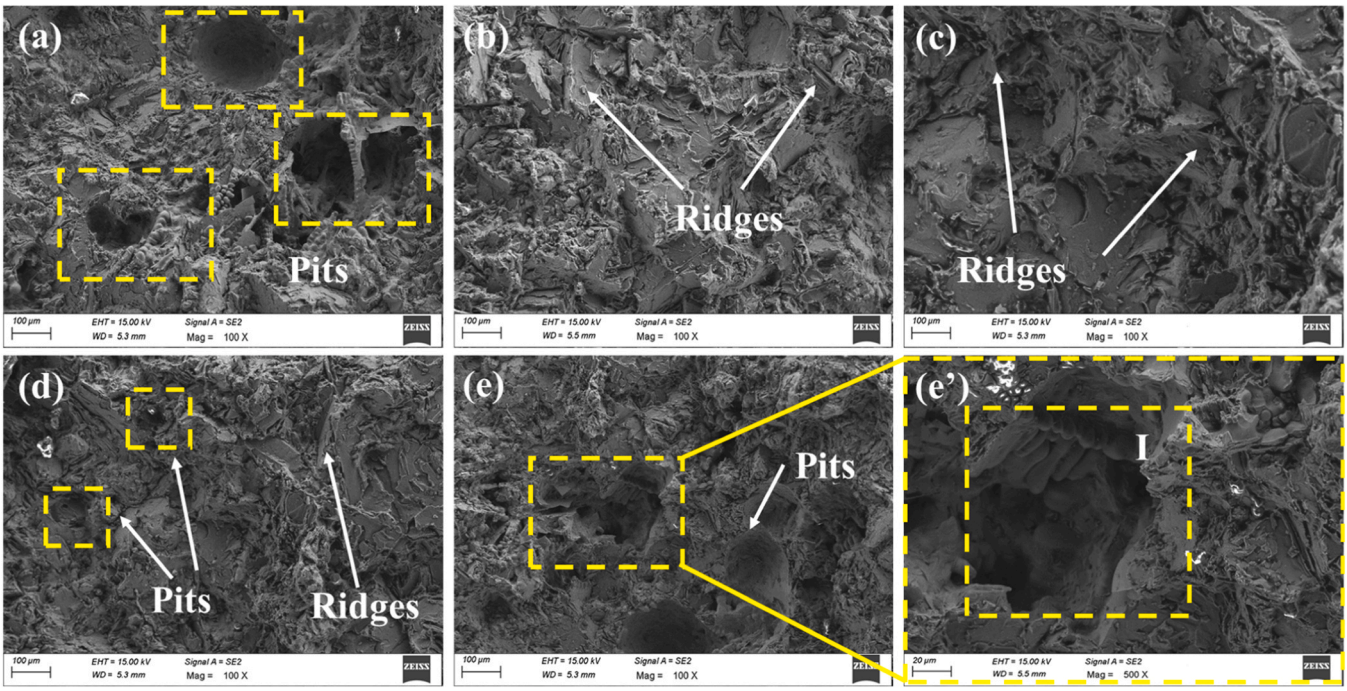

Fig. 12. Tensile fracture images of (a) Ti-6Al-4 V (b) 2 wt%-AlCoCrFeNi/Ti-6Al-4 V (c) 4 wt%-AlCoCrFeNi/Ti-6Al-4 V (d) 6 wt%-AlCoCrFeNi/Ti-6Al-4 V (e) 8 wt %-AlCoCrFeNi/Ti-6Al-4 V (e') magnified image of 8 wt%-AlCoCrFeNi/Ti-6Al-4 V.

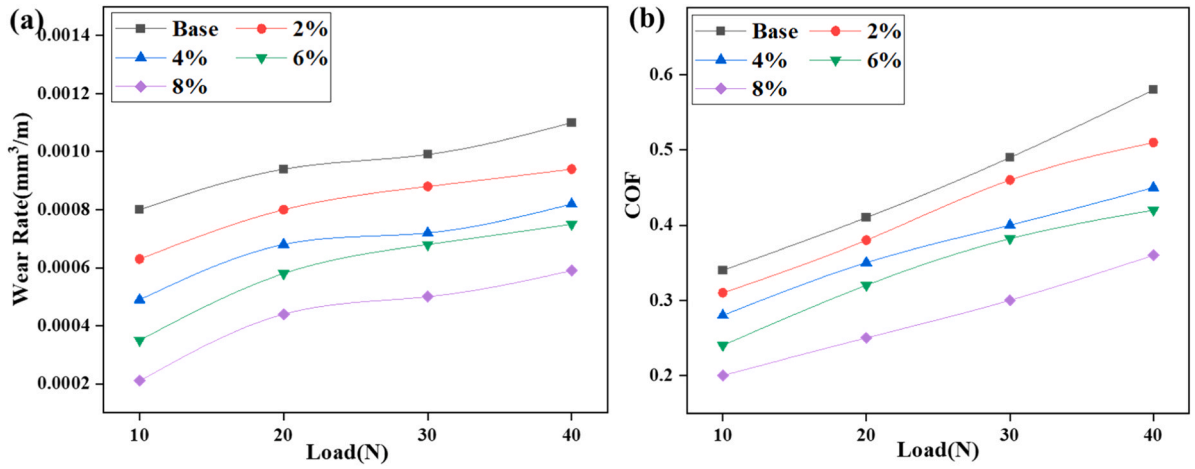

Fig. 13. (a) Wear rate and (b) COF profiles of base and reinforced samples under different loads.

Table 1
Decrease in wear rates and COF of AlCoCrFeNi reinforced samples at 40 N.

wt% reinforced	Decrease in wear rate	Decrease in COF
2 %	14.54 %	12 %
4 %	25.45 %	22.41 %
6 %	34.81 %	32.58 %
8 %	46.36 %	39.93 %

higher pressure applied to the contact region against the rotating disc leads to the disintegration of the sample surface, resulting in pronounced delamination and exhibits deep groove under an increased load of 40 N (Fig. 15). Therefore, the samples exhibited a maximum wear rate at 40 N load. Due to the increased hardness provided by the HEA reinforcement, the likelihood of adhesive wear diminishes. As a result, abrasive wear emerges as the predominant factor.

3.3.2. *Influence of sliding distance*

The impact of sliding distance on the wear rate and COF of the base and the reinforced samples were analyzed under a constant load of 10 N and sliding velocity of 0.5 m/s. Fig. 16 depicts the profiles of wear rate and COF, increasing with the incremental surge of the sliding distance for all the samples. All the samples exhibited a maximum wear rate at 1500 m where, 8 wt% AlCoCrFeNi/Ti-6Al-4 V exhibited the lowest wear rate of 5.7×10^{-4} mm^3/m at 1500 m sliding distance with a COF of 0.35. While the highest wear rate and COF of 9.9×10^{-4} mm^3/m and 0.55 were exhibited by the base sample at 1500 m. This shows a decrease of 43.61 % in wear rate. With an increase in the sliding distance to 2000 m, the samples were observed to have reduced wear, and the decrease in wear rates and COF of HEA reinforced samples at 2000 m sliding distance when compared to the base sample are mentioned in Table 2. In accordance with Archard's Law, the wear rate of the sample shows an inverse relationship with its hardness and a direct correlation with the sliding distance [52]. The base sample, characterized by its lower

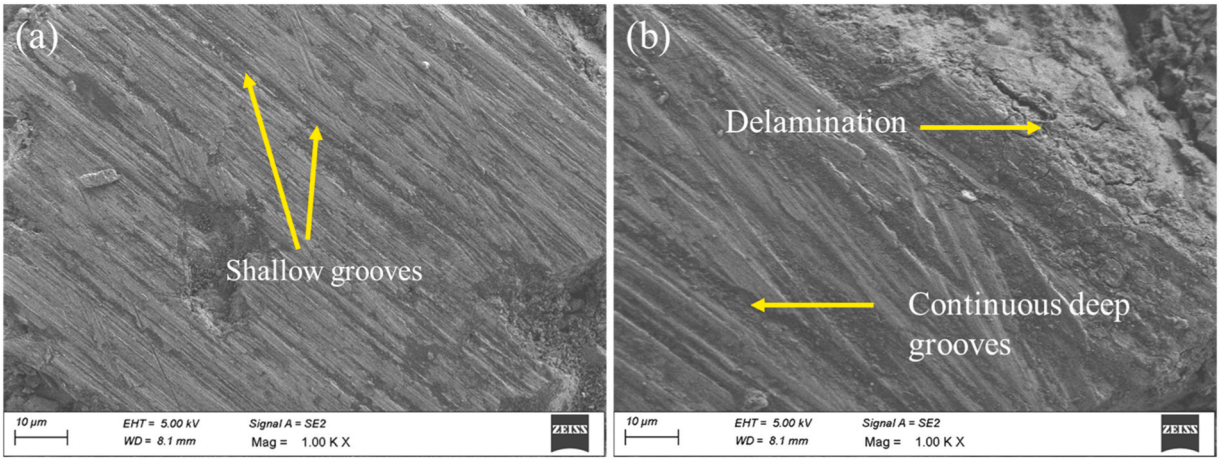

Fig. 14. Worn surface of 8 wt%AlCoCrFeNi/ Ti-6Al-4 V at (a) 10 N (b) 40 N.

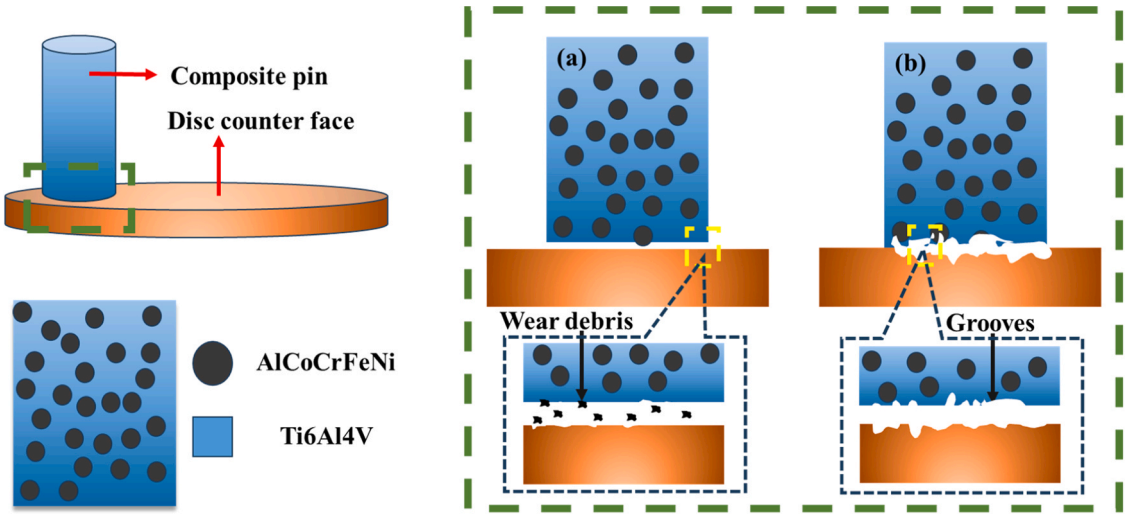

Fig. 15. Schematic representation of abrasive wear mechanism.

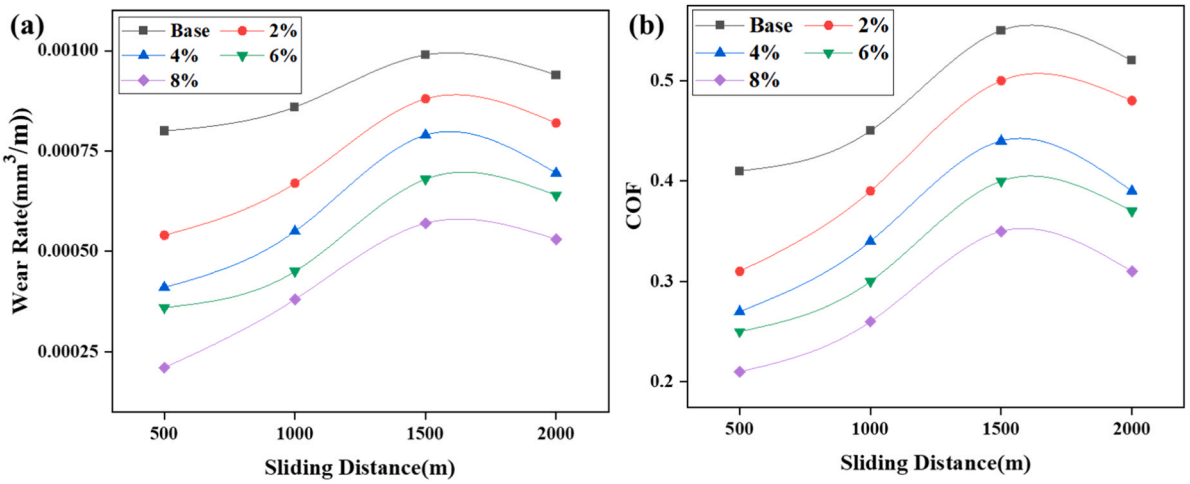

Fig. 16. (a) Wear rate and (b) COF profiles of base and reinforced samples under different sliding distance.

hardness, exhibited diminished resistance to wear, resulting in an elevated wear rate. The presence of elements like Al, and Ni in the HEA contributes to the high-strength and hardness of the reinforced samples when compared to the base. However, the wear rate is reduced when the sliding distance is increased further from 1500 m. The increase in wear rate for the first 1500 m happens due to the transfer of small flakes of the

Table 2
Decrease in wear rates and COFs of AlCoCrFeNi reinforced samples at 2000 m.

wt% reinforced	Decrease in wear rate	Decrease in COF
2 %	12.76 %	7.69 %
4 %	26.06 %	16.73 %
6 %	31.91 %	28.84 %
8 %	43.61 %	40.39 %

sample onto the disc. The small flakes that are hardened exhibit higher COF when they slide across the sample resulting in more removal of the materials thus increasing the wear rate [53]. The reduction in wear rate at 2000 m sliding distance is due to the formation of a mechanical mixed layer (MML). The HEA particles and debris produced due to wear roll between the pin-disc interface led to an oxide layer formation on the pin at elevated temperature, which in turn prevents higher material loss by reducing direct contact between the pin and disc. The presence of Al in the HEA with a BCC phase helps reduce the wear rate. The robust BCC phase's exceptional resistance to plastic deformation and delamination allows the oxide layer to withstand abrasion [54].

The SEM images of worn surfaces of 8 wt% AlCoCrFeNi reinforced Ti-6Al-4 V under 500 m and 2000 m sliding distances are illustrated in Fig. 17. The worn surface of the reinforced sample at 500 m sliding distance is illustrated in Fig. 17(a). Frictional heat, arising from the sliding contact between the pin and disc, played a part in the genesis of spallation. Additionally applying the load over a long period of time due to the low sliding velocity has caused localized plastic deformation along with stress concentration which has also contributed to the occurrence of spallation. This plastic deformation also led to the formation of grooves on the reinforced sample [55]. Fig. 17(b) shows the worn surface of the reinforced sample at the maximum sliding distance of 2000 m. As the sliding distance increased, the reinforced sample's elevated hardness resulted in heightened resistance against the rotating disc, causing observable surface distortion. The induced cyclic stresses and temperature along with debris produced from the pin that are formed because of increasing sliding distance, led to the formation of the oxide layer/MML which is also responsible for the decrease in friction (Fig. 18). The presence of the developed oxide layer on the contacting surface led to a reduction in wear rate and COF from 1500 m to 2000 m sliding distance [56].

3.3.3. *Influence of sliding velocity*

The wear rate and COF of the base and the reinforced samples under the incremental change of sliding velocity are demonstrated in Fig. 19. The sliding velocity was changed from 0.5 m/s to 3.5 m/s with an increment of 1 m/s under a constant load of 20 N and sliding distance of 500 m. The wear rate of the HEA reinforced samples was observed to be low compared to the wear rate of the base sample. The wear rate of the base sample and the reinforced samples increased linearly when the sliding velocity was changed incrementally from 0.5 m/s to 2.5 m/s. The minimum wear rate observed at 2.5 m/s was 5.7×10^{-4} mm^3/m exhibited by 8 wt% AlCoCrFeNi reinforced Ti-6Al-4 V along with a COF of 0.35 which revealed to have a significant decrement in wear rate by 45.19 % when compared to the base sample. Lower velocities result in the induction of high temperatures on the contact surface, driven by extended periods of contact with the disc. Hence, long periods of contact resulted in higher material loss, leading to a higher wear rate. The load-bearing effect of the HEA particles resulted in enhanced wear resistance than the base sample at similar conditions [57]. The wear rate and COF of the samples were reduced above 2.5 m/s due to MML formation. MML was developed by the delamination of the small flakes of material on the wear surface of the samples owing to high induced temperatures, shielding the samples from abrasive wear even as the sliding velocity was increased. The Ti matrix possesses a significant self-diffusion coefficient and properties related to allotropic crystal transformation, leading to reduced thermal conductivity within the matrix [58]. With the ongoing wear test, the accumulation of generated heat causes a gradual increase in the surface temperature of both the base sample and the reinforced samples. Upon reaching a particular temperature, the Ti-6Al-4 V matrix undergoes a chemical reaction with oxygen, leading to the generation of oxide layers. In Ti alloys, friction oxides are often perceived as lacking a protective effect on the matrix due to their thin and brittle nature [59,60]. Since the evenly distributed HEA particles are present in the reinforced samples, they can contribute to a refined supportive role and better resistance to wear resulted in low wear rates comparing with the base sample. Furthermore, the enhanced wear resistance is attributed to the better interfacial bonding and the hindrance of dislocation movement caused due to the HEA particle reinforcement. 8 wt% reinforced sample has a more homogenous distribution of the HEA particles compared to the other reinforced samples, which resulted in an enhanced reduction in wear rate. The decrease in wear rate of the HEA reinforced samples when compared to the base sample at 3.5 m/s sliding velocity has been mentioned in Table 3.

Fig. 20 reveals the worn surfaces of the 8 wt% AlCoCrFeNi reinforced Ti-6Al-4 V under 0.5 m/s and 3.5 m/s sliding velocities. The worn surface of the reinforced sample under minimum sliding velocity (0.5 m/s) has been illustrated in Fig. 20(a). The reinforced sample undergoes substantial thermal stress due to the elevated temperatures on the rubbing surfaces between the pin and disc. The elevated hardness of the reinforced sample enabled it to withstand thermal stress, enhancing its wear resistance and subsequently leading to an increase in traction force. This caused the surface to undergo plastic deformation and in turn

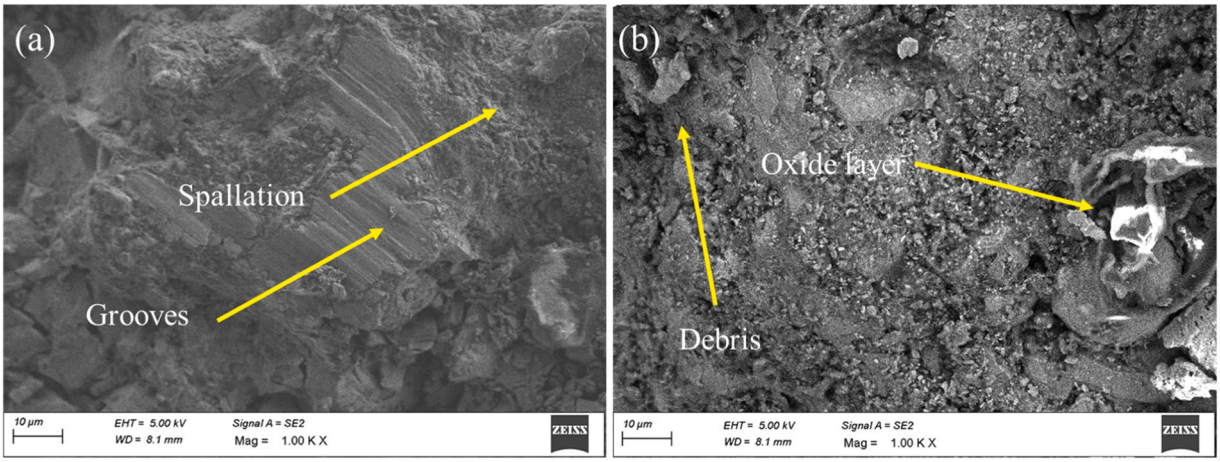

Fig. 17. Worn surface of 8 wt%AlCoCrFeNi/Ti-6Al-4 V at (a) 500 m (b) 2000 m.

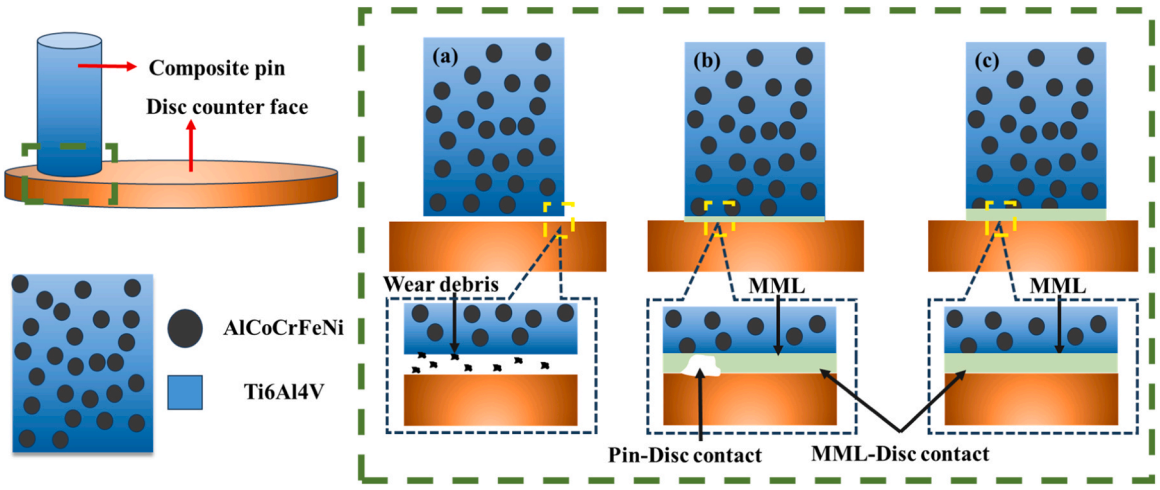

Fig. 18. Schematic representation of oxide layer/MML formation.

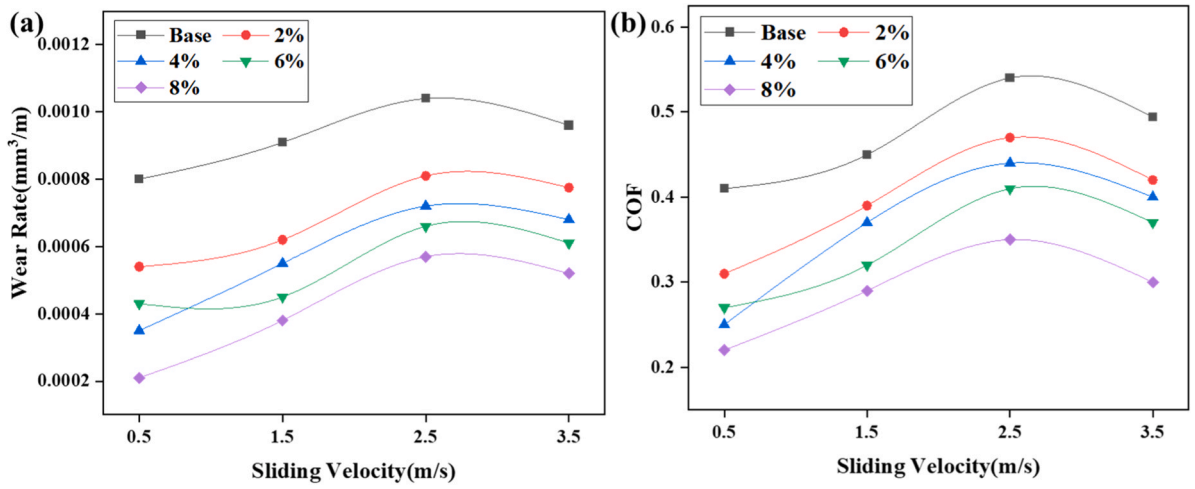

Fig. 19. (a) Wear rate and (b) COF profiles of base and reinforced samples under different sliding velocities.

Table 3
Decrease in wear rates and COF of AlCoCrFeNi reinforced samples at 3.5 m/s.

wt% reinforced	Decrease in wear rate	Decrease in COF
2 %	19.27 %	14.97 %
4 %	29.17 %	19.02 %
6 %	36.45 %	25.10 %
8 %	45.83 %	39.27 %

resulted in the formation of grooves, and spallation and made small flakes of reinforced sample detach from the surface. The grooves typically initiated by the traction force, tend to form along the direction of the sliding surface [61]. Fig. 20(b) represents the oxide layer formed on the surface of the reinforced sample as a result of high temperature induced by frictional heat at maximum sliding velocity (3.5 m/s) Thus, the oxide layer formation caused the decrease in wear rate. Al present in the base acts as the oxide layer promoter since Al is passive. The presence of an oxide layer serves as a lubricating barrier, inhibiting the direct contact between the mating surfaces and subsequently reducing friction between them [62,63].

4. Conclusion

In this study, the Ti-6Al-4 V matrix was reinforced with equiatomic AlCoCrFeNi, encompassing various weight percentages. The samples were fabricated through microwave sintering, leading to the following conclusions:

- The microstructural analysis of the HEA-reinforced samples revealed a uniform dispersion of HEA particles and a well-established interface bonding with the base sample, attributed to the application of microwave sintering. EBSD analysis showed the refined grain boundaries along with the grain distribution and crystal lattice orientation.
- In relation to the base sample, the reinforced samples exhibit minimal porosity, without much change in density. The microhardness was increased significantly with the inclusion of the reinforcement. The highest hardness value of 634HV was shown by 8 wt% AlCoCrFeNi/Ti-6Al-4 V which was 81.66 % when compared to the base sample. The tensile test also resulted in similar results having the 8 wt% AlCoCrFeNi/Ti-6Al-4 V exhibiting 21.23 % increment in the yield strength compared to the base sample.
- The wear rate and COF decreased in all the reinforced samples with an increment in the wt% of HEA reinforcement. The highest wear resistance was shown by 8 wt% AlCoCrFeNi/Ti-6Al-4 V which resulted in a decrease in wear rate by 45 % and COF by 40 % compared to the base sample.

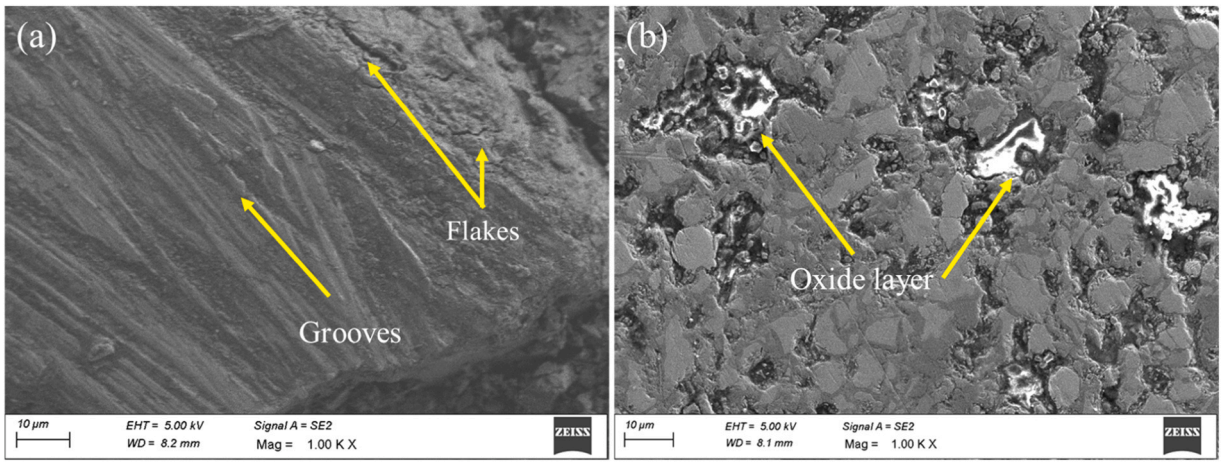

Fig. 20. Worn surface of 8 wt%AlCoCrFeNi/Ti-6Al-4 V at (a) 0.5 m/s (b) 3.5 m/s.

The introduction of AlCoCrFeNi has brought about substantial enhancements in the microstructural, mechanical, and tribological properties of Ti-6Al-4 V when compared to the base sample. An increase in hardness without much change in density shows the material potential to be applicable in aerospace industries for making structural parts, landing gear components, fasteners, satellite frames, panels, and mounting brackets. In addition, due to its high wear resistance and less friction, it can be used in the field of valves, and pumps. Further research in this area can be of testing the material under different environmental conditions, different heat treatments, numerical analysis for multiple environments and advancement in this field resulting in the commercialization of HEA reinforced Ti composites.

Funding

None.

CRediT authorship contribution statement

Mahesh Mandapalli: Formal analysis, Investigation, Writing – original draft. **U.V. Akhil:** Conceptualization, Investigation, Methodology, Validation, Writing – original draft. **N. Radhika:** Project administration, Supervision, Writing – review & editing. **L. Rajeshkumar:** Project administration, Supervision, Validation, Writing – review & editing.

Declaration of Competing Interest

The authors declare that they have no known competing financial interests or personal relationships that could have appeared to influence the work reported in this paper.

Data availability

The data cannot be shared as no data was used in the study.

References

[1] B.A. Khidhir, Y.M. Ahmed, K. Sahari, M. Ishak, K. Salleh, M. Sahari, A. Khidhir, Titanium and its alloy, Int. J. Sci. Res. (2014). ⟨https://www.researchgate.net/publication/267034976⟩.
[2] J.C. Williams, R.R. Boyer, Opportunities and issues in the application of titanium alloys for aerospace components, Metals 10 (2020), https://doi.org/10.3390/met10060705.
[3] J. Zhang, X. Li, D. Xu, R. Yang, Recent progress in the simulation of microstructure evolution in titanium alloys, Prog. Nat. Sci. Mater. Int. 29 (2019) 295–304, https://doi.org/10.1016/j.pnsc.2019.05.006.
[4] B. Narayanan, A. Rajamanickam, A Review on Tribological Behaviour of Titanium Alloys, n.d. ⟨http://www.ijpam.eu⟩.
[5] M. Fellah, M. Labaïz, O. Assala, L. Dekhil, A. Taleb, H. Rezag, A. Iost, Tribological behavior of Ti-6Al-4V and Ti-6Al-7Nb alloys for total hip prosthesis, Adv. Tribol. 2014 (2014), https://doi.org/10.1155/2014/451387.
[6] M. Mehdi, K. Farokhzadeh, A. Edrisy, Dry sliding wear behavior of superelastic Ti-10V–2Fe-3Al β-titanium alloy, Wear 350–351 (2016) 10–20, https://doi.org/10.1016/j.wear.2015.12.006.
[7] M.D. Hayat, H. Singh, Z. He, P. Cao, Titanium metal matrix composites: an overview, Compos. Part A Appl. Sci. Manuf. 121 (2019) 418–438, https://doi.org/10.1016/j.compositesa.2019.04.005.
[8] R. Shetty, A. Hegde, U.K. Shetty SV, R. Nayak, N. Naik, M. Nayak, Processing and mechanical characterisation of titanium metal matrix composites: a literature review, J. Compos. Sci. 6 (2022), https://doi.org/10.3390/jcs6120388.
[9] M. Mashabela, M. Maringa, T. Dzogbewu, Nanoparticulate reinforced composites and their application to additively manufactured TI6AL4V for use in the aerospace sector, Manuf. Rev. 9 (2022), https://doi.org/10.1051/mfreview/2022027.
[10] H. Attar, S. Ehtemam-Haghighi, D. Kent, M.S. Dargusch, Recent developments and opportunities in additive manufacturing of titanium-based matrix composites: a review, Int. J. Mach. Tools Manuf. 133 (2018) 85–102, https://doi.org/10.1016/j.ijmachtools.2018.06.003.
[11] Y. Guo, K. Yu, J. Niu, M. Sun, G. Dai, Z. Sun, H. Chang, Effect of reinforcement content on microstructures and mechanical properties of graphene nanoflakes-reinforced titanium alloy matrix composites, J. Mater. Res. Technol. 15 (2021) 6871–6882, https://doi.org/10.1016/j.jmrt.2021.11.109.
[12] X. Gao, X. Lin, Q. Yan, Z. Wang, X. Yu, Y. Zhou, Y. Hu, W. Huang, Effect of Cu content on microstructure and mechanical properties of in-situ β phases reinforced Ti/Zr-based bulk metallic glass matrix composite by selective laser melting (SLM), J. Mater. Sci. Technol. 67 (2021) 174–185, https://doi.org/10.1016/j.jmst.2020.06.024.
[13] D.K. Ammisetti, S.S. Harish Kruthiventi, Recent trends on titanium metal matrix composites: a review, Mater. Today Proc. (2019) 9730–9735, https://doi.org/10.1016/j.matpr.2020.08.732. Elsevier Ltd.
[14] S. Li, K. Kondoh, H. Imai, B. Chen, L. Jia, J. Umeda, Microstructure and mechanical properties of P/M titanium matrix composites reinforced by in-situ synthesized TiC-TiB, Mater. Sci. Eng. A 628 (2015) 75–83, https://doi.org/10.1016/j.msea.2015.01.033.
[15] Y. Hu, W. Cong, X. Wang, Y. Li, F. Ning, H. Wang, Laser deposition-additive manufacturing of TiB-Ti composites with novel three-dimensional quasi-continuous network microstructure: effects on strengthening and toughening, Compos. B Eng. 133 (2018) 91–100, https://doi.org/10.1016/j.compositesb.2017.09.019.
[16] Y. Hu, W. Cong, A review on laser deposition-additive manufacturing of ceramics and ceramic reinforced metal matrix composites, Ceram. Int. 44 (2018) 20599–20612, https://doi.org/10.1016/j.ceramint.2018.08.083.
[17] Y. Jiao, L. Huang, L. Geng, Progress on discontinuously reinforced titanium matrix composites, J. Alloy. Compd. 767 (2018) 1196–1215, https://doi.org/10.1016/j.jallcom.2018.07.100.
[18] F. Zhou, H. Zhang, C. Sun, J. Dai, Microstructure and wear properties of multi ceramics reinforced metal-matrix composite coatings on Ti–6Al–4V alloy fabricated by laser surface alloying, Surf. Eng. 35 (2019) 683–691, https://doi.org/10.1080/02670844.2019.1570611.
[19] Wasim Jamshed Sami Ullah Khan, Finite element analysis and wear rate analysis of nano coated high speed steel tools for industrial application, Babylon. J. Mech. Eng. 2023 (2023) 13–19, https://doi.org/10.58496/bjme/2023/002.
[20] S.A. Krishna, N. Noble, N. Radhika, B. Saleh, A comprehensive review on advances in high entropy alloys: fabrication and surface modification methods, properties, applications, and future prospects, J. Manuf. Process. 109 (2024) 583–606, https://doi.org/10.1016/J.JMAPRO.2023.12.039.
[21] Q. Chang, Y. Liu, Y. Xia, S. Barman, K.Kumar Gupta, S. Dey, Enhancing mechanical performance of Al0.3CoCrFeNi HEA films through graphene coating: insights from nanoindentation and dislocation mechanism analysis, Model. Simul. Mater. Sci. Eng. 32 (2024) 035012, https://doi.org/10.1088/1361-651X/AD2789.

[22] D.B. Miracle, O.N. Senkov, A critical review of high entropy alloys and related concepts, Acta Mater. 122 (2017) 448–511, https://doi.org/10.1016/j.actamat.2016.08.081.
[23] J.C. Rao, V. Ocelík, D. Vainchtein, Z. Tang, P.K. Liaw, J.T.M. De Hosson, The fcc-bcc crystallographic orientation relationship in AlxCoCrFeNi high-entropy alloys, Mater. Lett. 176 (2016) 29–32, https://doi.org/10.1016/j.matlet.2016.04.086.
[24] Y. Chen, S. Zhu, X. Wang, B. Yang, G. Han, L. Qiu, Microstructure evolution and strengthening mechanism of Al0.4CoCu0.6NiSix (x=0–0.2) high entropy alloys prepared by vacuum arc melting and copper injection fast solidification, Vacuum 150 (2018) 84–95, https://doi.org/10.1016/j.vacuum.2018.01.031.
[25] Y. Tong, Z. Ren, Y. Hu, H. Huang, X. Zhang, X. Ji, P. Zhang, M. Zhang, Microstructure and properties of CoCrNiFeMnAl0.5 high-entropy alloys prepared by gas atomization combined with oscillatory pressure sintering, Intermetallics 143 (2022), https://doi.org/10.1016/j.intermet.2022.107460.
[26] N.G. Kipkirui, T.T. Lin, R.S. Kiplangat, S.H. Chen, Study of the stabilization process of gas atomized Al0.5CoCrFeNi2Ti0.5 high-entropy alloy in phase transformation, J. Alloy. Compd. 905 (2022), https://doi.org/10.1016/j.jallcom.2022.164230.
[27] M. Vaidya, G.M. Muralikrishna, B.S. Murty, High-entropy alloys by mechanical alloying: a review, J. Mater. Res. 34 (2019) 664–686, https://doi.org/10.1557/jmr.2019.37.
[28] S.N. Kishan, R.A. Sree, U.V. Akhil, N. Radhika, Electrochemical and hot corrosion analysis of novel AlBeSiTiV light weight HEA coating on SS316, Phys. Scr. (2024), https://doi.org/10.1088/1402-4896/AD1F18.
[29] T. Lu, W. Chen, Z. Li, T. He, B. Li, R. Li, Z. Fu, S. Scudino, Processing and mechanical properties of fine grained Al matrix composites reinforced with a uniform dispersion of nanocrystalline high-entropy alloy particles, J. Alloy. Compd. 801 (2019) 473–477, https://doi.org/10.1016/j.jallcom.2019.06.157.
[30] S.A. McEnroe, R.J. Harrison, M.J. Jackson, al -, K. Mutombo, Research and development of Ti and Ti alloys: past, present and future, IOP Conf. Ser. Mater. Sci. Eng. 430 (2018) 012007, https://doi.org/10.1088/1757-899X/430/1/012007.
[31] C. Romero, F. Yang, L. Bolzoni, Fatigue and fracture properties of Ti alloys from powder-based processes – a review, Int. J. Fatigue 117 (2018) 407–419, https://doi.org/10.1016/J.IJFATIGUE.2018.08.029.
[32] C. Singhal, Q. Murtaza, Microwave sintering of advanced composites materials: a review, 2018, Mater. Today Proc. (2018).
[33] U.V. Akhil, N. Radhika, T. Ramkumar, A. Pramanik, Effect of graphene on the tribological behavior of Ti6Al6V2Sn/Gn composite produced via microwave sintering, Int. J. Lightweight Mater. Manuf. 7 (2024) 1–13, https://doi.org/10.1016/J.IJLMM.2023.10.001.
[34] P. Muthusamy, M. Mohanraj, T. Ramkumar, M. Selvakumar, Effect of microwave sintering on the microstructure and tribological behavior of Ti-3Al-2.5 V-xWC composite, Tribol. Int. 174 (2022), https://doi.org/10.1016/j.triboint.2022.107714.
[35] E. Breval, J.P. Cheng, D.K. Agrawal, P. Gigl, M. Dennis, R. Roy, A.J. Papworth, Comparison between microwave and conventional sintering of WC/Co composites, Mater. Sci. Eng. A 391 (2005) 285–295, https://doi.org/10.1016/j.msea.2004.08.085.
[36] M. Madhan, G. Prabhakaran, Microwave versus conventional sintering: microstructure and mechanical properties of Al2O3-SiC ceramic composites, Bol. Soc. Esp. Ceram. Vidr. 58 (2019) 14–22, https://doi.org/10.1016/j.bsecv.2018.06.001.
[37] H. Yang, X. Zhou, J. Yu, H. Wang, Z. Huang, Microwave and conventional sintering of SiC/SiC composites: flexural properties and microstructures, Ceram. Int. 41 (2015) 11651–11654, https://doi.org/10.1016/j.ceramint.2015.05.126.
[38] Y.A. Alshataif, S. Sivasankaran, F.A. Al-Mufadi, A.S. Alaboodi, H.R. Ammar, Manufacturing methods, microstructural and mechanical properties evolutions of high-entropy alloys: a review, Met. Mater. Int. 26 (2020) 1099–1133, https://doi.org/10.1007/s12540-019-00565-z.
[39] G. Hillel, L. Natovitz, S. Salhov, S. Haroush, M. Pinkas, L. Meshi, Understanding the role of the constituting elements of the alcocrfeni high entropy alloy through the investigation of quaternary alloys, Metals 10 (2020) 1–11, https://doi.org/10.3390/met10101275.
[40] P. Amit, I. Sushil, Machining challenges in Ti-6Al-4V.-A review, Int. J. Innov. Eng. Technol. (2015). ⟨https://www.researchgate.net/publication/283290011⟩.
[41] P. Bocchetta, L.Y. Chen, J.D.C. Tardelli, A.C. Dos Reis, F. Almeraya-Calderón, P. Leo, Passive layers and corrosion resistance of biomedical ti-6al-4v and β-ti alloys, Coatings 11 (2021), https://doi.org/10.3390/coatings11050487.
[42] K.R. Ramkumar, S. Sivasankaran, F.A. Al-Mufadi, S. Siddharth, R. Raghu, Investigations on microstructure, mechanical, and tribological behaviour of AA 7075–x wt% TiC composites for aerospace applications, Arch. Civ. Mech. Eng. 19 (2019) 428–438, https://doi.org/10.1016/j.acme.2018.12.003.
[43] S. Najafi, A.R. Eivani, M. Samaee, H.R. Jafarian, J. Zhou, A comprehensive investigation of the strengthening effects of dislocations, texture and low and high angle grain boundaries in ultrafine grained AA6063 aluminum alloy, Mater. Charact. 136 (2018) 60–68, https://doi.org/10.1016/j.matchar.2017.12.004.
[44] B. Gu, P. Chekhonin, S.W. Xin, G.Q. Liu, C.L. Ma, L. Zhou, W. Skrotzki, Effect of temperature and strain rate on the deformation behavior of Ti5321 during hot-compression, J. Alloy. Compd. 876 (2021), https://doi.org/10.1016/j.jallcom.2021.159938.
[45] S. Joseph, K. Joseph, T.C. Lindley, D. Dye, The role of dwell hold on the dislocation mechanisms of fatigue in a near alpha titanium alloy, Int. J. Plast. 131 (2020), https://doi.org/10.1016/j.ijplas.2020.102743.
[46] Z. Yuan, H. Liu, Z. Ma, X. Ma, K. Wang, X. Zhang, Microstructure and properties of high entropy alloy reinforced titanium matrix composites, Mater. Charact. 187 (2022), https://doi.org/10.1016/j.matchar.2022.111856.
[47] Y. Xiong, F. Zhang, Y. Huang, C. Shang, Q. Wan, Multiple strengthening via high-entropy alloy particle addition in titanium matrix composites fabricated by spark plasma sintering, Mater. Sci. Eng. A 859 (2022), https://doi.org/10.1016/j.msea.2022.144235.
[48] B.J. Lv, S. Wang, T.W. Xu, F. Guo, Effects of minor Nd and Er additions on the precipitation evolution and dynamic recrystallization behavior of Mg–6.0Zn–0.5Mn alloy, J. Magnes. Alloy. 9 (2021) 840–852, https://doi.org/10.1016/j.jma.2020.06.018.
[49] S.M. Rafiaei, A. Bahrami, M. Shokouhimehr, Influence of Ni/Co binders and Mo2C on the microstructure evolution and mechanical properties of (Ti0.93W0.07) C–based cermets, Ceram. Int. 44 (2018) 17655–17659, https://doi.org/10.1016/j.ceramint.2018.06.227.
[50] A. Bahrami, A. Miroux, J. Sietsma, Modeling of strain hardening in the aluminum alloy AA6061, Metall. Mater. Trans. A Phys. Met. Mater. Sci. (2013) 2409–2417, https://doi.org/10.1007/s11661-012-1594-6.
[51] S. Ragunath, N. Radhika, S. Aravind Krishna, N. Jeyaprakash, Enhancing microstructural, mechanical and tribological behaviour of AlSiBeTiV high entropy alloy reinforced SS410 through friction stir processing, Tribol. Int. 188 (2023), https://doi.org/10.1016/j.triboint.2023.108840.
[52] J. Hu, H. Song, S. Sandfeld, X. Liu, Y. Wei, Breakdown of Archard law due to transition of wear mechanism from plasticity to fracture, Tribol. Int. 173 (2022), https://doi.org/10.1016/j.triboint.2022.107660.
[53] A. Pramanik, Effects of reinforcement on wear resistance of aluminum matrix composites, Trans. Nonferrous Met. Soc. China (Engl. Ed.) 26 (2016) 348–358, https://doi.org/10.1016/S1003-6326(16)64125-0.
[54] N. Noble, N. Radhika, M. Sathishkumar, B. Saleh, Characterisation and property evaluation of High Entropy Alloy coating on 316L steel via thermal spray synthesis, Tribol. Int. 185 (2023) 108525, https://doi.org/10.1016/J.TRIBOINT.2023.108525.
[55] K.-H. Zum Gahr, Wear by Hard Particles, 1998.
[56] X. Guo, I. Baker, F.E. Kennedy, M. Song, A comparison of the dry sliding wear behavior of NiCoCr medium entropy alloy with 316 stainless steel, Mater. Charact. 160 (2020), https://doi.org/10.1016/j.matchar.2020.110132.
[57] X. Yang, Z. Yan, P. Dong, B. Cheng, J. Zhang, T. Zhang, H. Zhang, W. Wang, Surface modification of aluminum alloy by incorporation of AlCoCrFeNi high entropy alloy particles via underwater friction stir processing, Surf. Coat. Technol. 385 (2020), https://doi.org/10.1016/j.surfcoat.2020.125438.
[58] J. Jin, S. Zhou, Y. Zhao, Q. Zhang, X. Wang, W. Li, D. Chen, L.C. Zhang, Refined microstructure and enhanced wear resistance of titanium matrix composites produced by selective laser melting, Opt. Laser Technol. 134 (2021), https://doi.org/10.1016/j.optlastec.2020.106644.
[59] Q.Y. Zhang, Y. Zhou, L. Wang, X.H. Cui, S.Q. Wang, Investigation on tribo-layers and their function of a titanium alloy during dry sliding, Tribol. Int. 94 (2016) 541–549, https://doi.org/10.1016/j.triboint.2015.10.018.
[60] A. Sabahi Namini, S.A.A. Dilawary, A. Motallebzadeh, M. Shahedi Asl, Effect of TiB2 addition on the elevated temperature tribological behavior of spark plasma sintered Ti matrix composite, Compos. B Eng. 172 (2019) 271–280, https://doi.org/10.1016/j.compositesb.2019.05.073.
[61] Y. Li, Y. Shi, Microhardness, wear resistance, and corrosion resistance of AlxCrFeCoNiCu high-entropy alloy coatings on aluminum by laser cladding, Opt. Laser Technol. 134 (2021), https://doi.org/10.1016/j.optlastec.2020.106632.
[62] M. Garg, H.S. Grewal, R.K. Sharma, H.S. Arora, Enhanced oxidation resistance of ultrafine-grain microstructure AlCoCrFeNi high entropy alloy, ACS Omega 7 (2022) 12589–12600, https://doi.org/10.1021/acsomega.1c06014.
[63] A. Meghwal, A. Anupam, V. Luzin, C. Schulz, C. Hall, B.S. Murty, R.S. Kottada, C. C. Berndt, A.S.M. Ang, Multiscale mechanical performance and corrosion behaviour of plasma sprayed AlCoCrFeNi high-entropy alloy coatings, J. Alloy. Compd. 854 (2021), https://doi.org/10.1016/j.jallcom.2020.157140.